São Paulo State University

Graduate Program on Cartographic Sciences

Mariana Bardella Thomaz

UAV HYPERSPECTRAL IMAGES CORRECTED OF ILLUMINATION DIFFERENCES CONSIDERING MICROTOPOGRAPHY IN CORRECTION MODELS

Presidente Prudente

2020

UAV HYPERSPECTRAL IMAGES CORRECTED OF ILLUMINATION DIFFERENCES CONSIDERING MICROTOPOGRAPHY IN CORRECTION MODELS

Dissertation submitted to the Faculty of Science and Technology of São Paulo State University (UNESP) in fulfillment of the requirements for the degree Master of Cartographic Sciences

Advisor: Prof. Dr. Nilton N. Imai

Co-advisor: Prof. Dr. Antônio M. G. Tommaselli

PRESIDENTE PRUDENTE

2020

T465u

Thomaz, Mariana Bardella
UAV hyperspectral images corrected of illumination differences considering microtopography in correction models / Mariana Bardella Thomaz. -- Presidente Prudente, 2020
79 f. : tabs., fotos, mapas

Dissertação (mestrado) - Universidade Estadual Paulista (Unesp), Faculdade de Ciências e Tecnologia, Presidente Prudente
Orientador: Nilton Nobuhiro Imai
Coorientador: Antonio Maria Garcia Tommaselli

1. Correção topográfica. 2. UAV. 3. BRDF. 4. Anisotropia. 5. Correção de Iluminação. I. Título.

Sistema de geração automática de fichas catalográficas da Unesp. Biblioteca da Faculdade de Ciências e Tecnologia, Presidente Prudente. Dados fornecidos pelo autor(a).

UNIVERSIDADE ESTADUAL PAULISTA

Câmpus de Presidente Prudente

CERTIFICADO DE APROVAÇÃO

TÍTULO DA DISSERTAÇÃO: UAV Hyperspectral Images corrected of illumination differences considering microtopography in correction models

AUTORA: MARIANA BARDELLA THOMAZ
ORIENTADOR: NILTON NOBUHIRO IMAI
COORIENTADOR: ANTONIO MARIA GARCIA TOMMASELLI

Aprovada como parte das exigências para obtenção do Título de Mestra em CIÊNCIAS CARTOGRÁFICAS, área: Aquisição, Análise e Representação de Informações Espaciais pela Comissão Examinadora:

Prof. Dr. NILTON NOBUHIRO IMAI
Departamento de Cartografia / Faculdade de Ciencias e Tecnologia de Presidente Prudente

Prof. Dr. ERIVALDO ANTONIO DA SILVA **(PARTICIPAÇÃO VIA VIDEOCONFERÊNCIA)**
Departamento de Cartografia / Faculdade de Ciencias e Tecnologia de Presidente Prudente

Prof. Dr. RUBENS AUGUSTO CAMARGO LAMPARELLI **(PARTICIPAÇÃO VIA VIDEOCONFERÊNCIA)**
Faculdade de Engenharia Agrícola / Universidade Estadual de Campinas

Presidente Prudente, 29 de abril de 2020

ACKNOWLEDGEMENTS

Pai, Luiz, todas as oportunidades que eu tive desde criança até hoje foram possíveis porque eu tive o seu apoio. Você dedicou sua vida toda para tornar meus sonhos possíveis, e eu sei que esse é o maior amor que eu já experimentei na vida. Mãe, Beatriz, sonhamos juntas esse sonho e sei que você nunca me deixou. Todos os dias me esforço para ser um pouco do que você foi como mulher, amiga e irmã. Você foi a pessoa mais criativa e resiliente que eu conheci. Obrigada pelo exemplo!

Lucas e Vitor, obrigada por caminharem comigo todo o tempo e serem irmãos protetores, incentivadores e compreensivos. Vocês fazem parte de quem eu sou e foram peças chave dessa trajetória acadêmica. Annelisa e Fernanda, que alegria ter vocês! E que sorte encontrar em vocês grandes amigas para partilhar da vida.

Germano, obrigada pelo apoio, pelo incentivo, pelo carinho e por acreditar que eu sou muito capaz. Você sempre colocou meus pés no chão e mostrou como encarar o mestrado de forma séria e dedicada. Muito disso pelo seu exemplo.

Tia Sandra, estivemos todos os dias juntas mesmo com tanta distância. E o seu carinho e apoio são coisas que fazem a vida mais colorida e leve! Obrigada por ser tão presente e querida.

Gabs (Gabriela T. Myioshi) como eu disse muitas vezes, aqui deixo eternizado: não sei o que seria de mim sem você! Obrigada! Você me ajudou em todos os aspectos e ensinou muito sobre sensoriamento remoto, fotogrametria e bondade de coração! Caio (Caio F. M. Fontoura Jr), obrigada pelo suporte em todo o mestrado! Você foi essencial para eu não me perder nas cobranças e chateações intrínsecas ao mestrado. Denise, minha amiga, você é um tesouro que encontrei, obrigada por mais essa caminhada juntas. Amanda, você faz questão de ser presente, isso já diz tudo. Obrigada por tanto.

Amigos da turma mestrado 2018: Aline, Caio, Letícia, Mariana, Melina, Renan, Viviane, Nelson, Weverton e Rafael vocês foram parte importantíssima do meu aprendizado nas ciências cartográficas, obrigada!

Matheus (IC) Fachin e Patrícia Matsumoto, obrigada por partilharem tantas vezes comigo sobre a vida na academia e me olharem com olhos tão doces, afetuosos e humanos.

Prof. Antônio Tommaselli, obrigada por, ainda em 2017, me acolher no programa, propor desafios e acreditar no meu potencial. Sua orientação e o conhecimento me fizeram crescer intelectualmente, profissionalmente e pessoalmente.

Prof. Nilton Imai, obrigada por depositar confiança em mim e me orientar pelos caminhos do sensoriamento remoto. Acima disso, obrigada por seu incentivo foi constante. Levarei comigo tudo que me ensinou!

UNESP, Programa de Pós-Graduação em Ciências Cartográficas, Corpo Docente e Discente, à vocês minha eterna gratidão por me formarem uma profissional qualificada e consciente do meu papel na sociedade.

AGRADECIMENTO FINANCEIRO:

Este Trabalho foi financiado em parte pela Coordenação de Aperfeiçoamento de Pessoal de Nível Superior – Brasil (CAPES) – Código de Financiamento 001.

Este trabalho foi financiado em parte pelo Conselho Nacional de Desenvolvimento Científico e Tecnológico – Brasil (CNPq) – Código de Financiamento nº 132467/2018-6

This study was financed in part by the Coordenação de Aperfeiçoamento de Pessoal de Nível Superior – Brasil (CAPES) – Finance Code 001

This study was financed in part by the Conselho Nacional de Desenvolvimento Científico e Tecnológico – Brasil (CNPq) – Finance Code n° 132467/2018-6

“I stand on the sacrifices of a million women before me thinking: what can I do to make this mountain taller so the women after me can see farther?”

Rupi Kaur

ABSTRACT

Use of UAV in remote sensing is a growing area of knowledge and pressed the development of lightweight multi and hyperspectral cameras, which could be used on board of UAV. Since the spectral information depends on the lighting condition of the scene, UAV acquired images demands research to assess image processing to better adapt the concepts already stablished to orbital images. Therefore, the radiometric correction is of main importance for data extraction from imagery with high confidence, once it is known that the reflectance factor is a function of geometric structure, solar angle and optical properties. In this regard, methodologies were developed to correct images from illumination differences, using the Bidirectional Reflectance Distribution Functions and the Topographic Correction Models, also known as illumination correction. This Work uses Rikola hyperspectral camera onboard of a UAV in tropical latitudes. It assesses how the anisotropy can influence variability in reflectance of targets, and how topographic correction models can be applied, using micro topography, to attenuate these effects. Three tests were done to study i) the view geometries of Rikola Hyperspectral camera and the no-Nadir data availability, ii) the variation of Anisotropy Factor between targets in the many view geometries and iii) Microtopography correction models to correct illumination differences using a highly detailed DSM (10 cm and 3 cm) to assess the micro relief. We applied the correction models in a forest area and in a controlled flight using a special target. Results show that the Rikola camera has restricted instantaneous field of view, entailing a low variability of viewing angles. The non-nadir angles reflectance factor showed no dependence of view angles and no relation with anisotropy. Concerning the correction models, the best outcome was using the more detailed DSM of 3 cm, which had high performance in minimizing the differences between the same target in different slope and aspect angles. Improvement of data reaches up to 93%.

Key-words: Topographic Correction, UAV, BRDF, Anisotropy, Illumination Correction

RESUMO

O uso do UAV no sensoriamento remoto é uma área crescente de conhecimento e pressionou o desenvolvimento de câmeras multi e hiperespectrais leves, que poderiam ser usadas embarcadas em UAV. Como as informações espectrais dependem das condições de iluminação da cena, as imagens adquiridas por UAV exigem pesquisa para avaliar o processamento de imagens para melhor adaptar os conceitos já estabelecidos às imagens orbitais. Portanto, a correção radiométrica é de fundamental importância para a extração de dados de imagens com alta confiança, uma vez que se sabe que o fator de refletância é uma função da estrutura geométrica, ângulo solar e propriedades ópticas. Nesse sentido, foram desenvolvidas metodologias para corrigir imagens das diferenças de iluminação, utilizando as Funções de Distribuição de Refletância Bidirecional e os Modelos de Correção Topográfica, também conhecidos como correção de iluminação. Este trabalho utiliza a câmera hiperespectral Rikola a bordo de um UAV em latitudes tropicais. Ele avalia como a anisotropia pode influenciar a variabilidade na reflectância dos alvos e como os modelos de correção topográfica podem ser aplicados, usando a micro topografia, para atenuar esses efeitos. Três testes foram realizados para estudar i) as geometrias de visada da câmera hiperespectral Rikola e a disponibilidade de dados fora do Nadir, ii) a variação do fator de anisotropia entre os alvos nas geometrias de visada e iii) modelos de correção de microtopografia para corrigir diferenças de iluminação utilizando um DSM muito detalhado (10 cm e 3 cm) para avaliar o micro-relevo. Aplicamos os modelos de correção em uma área de floresta e em um vôo controlado usando um alvo especial. Os resultados mostram que a câmera Rikola tem um pequeno IFOV, implicando baixa variabilidade dos ângulos de visada. O fator de reflectância dos ângulos não-nadir não mostrou dependência dos ângulos de visada e também não mostrou relação com a anisotropia. Em relação aos modelos de correção, o melhor resultado foi obtido através do uso do DSM mais detalhado de 3 cm, com alto desempenho em minimizar as diferenças entre o mesmo alvo em diferentes ângulos de inclinação e de aspecto. A performance dos modelos chega a 93%.

Palavras-chave: Correção Topográfica, UAV, BRDF, Anisotropia, Correção de Iluminação

LIST OF FIGURES

LIST OF TABLES

LIST OF ABBREVIATIONS AND SYMBOLS

ANIF	Anisotropy Factor
ANIX	Anisotropy Index
B	Band
BRDF	Bidirectional Reflectance Distribution Function
BRF	Bidirectional Reflectance Factor
DN	Digital Number
DSM	Digital Surface Model
Ei	Incident Irradiance
EMR	Electromagnetic Radiation
FOV	Field Of View
FPI	Fabry-Perrót Interferometer
FWHM	Full Width at Half Maximum
GSD	Ground Sample Distance
IL	Illumination
ILm	Medium Illumination
IR	Infra Red
Lr	Radiance Reflected
MDF	Medium Density Fiberboard
MOD1	Simple Ratio Model
MOD2	Cosine Model
MOD3	Normalized Model
NIR	Near Infra-Red
P1	Position 1
P2	Position 2
P3	Position 3
P4	Position 4
px	Pixel
R	Energy Reflected
Rad Target	Radiance of Target Before Correction
RPA	Remotely Piloted Aircraft
RT	Radiometric Target
SfM	Structure From Motion
STD	Standard Deviation
T	Board of The Radiometric Target
TIN	Triangulated Irregular Network
UAS	Unmaned Aerial System
UAV	Unmaned Aerial Vehicle
WS	Wet Soil
Φ	Radiant Flux [Watts]
λ	Wavelenght
θ	Zenith Angle
φ	Azimuth Angle

IL	Illumination
θ_0	Solar Zenith Angle
Φ_0	Solar Azimuth Angle
Φ_n	Aspect
θ_n	Slope
L_c	Corrected Factor
L_0	Pixel Value Before Correction
R_0	Reflectance in Nadir
R_{max}	Maximum Reflectance Factor
R_{min}	Minimum Reflectance Factor

SUMMARY

1. INTRODUCTION

Since the beginning of the development of Unmanned Aerial Vehicles (UAV), they have changed the way remote sensing is understood. Because of their easy adaptation, they have gained prominence in many fields, in both academic and commercial uses (PAJARES, 2015; YAO, QIN; CHEN, 2019). UAV platforms offer opportunities to obtain data from almost any place and can operate in cloudy days, depending on the application, once it can fly underneath the clouds. Both spatial and temporal resolutions can be adapted to the users needs. One of the biggest limiting factors, on the other hand, is the restricted sensor payload according to the UAV capacity (COLOMINA; MOLINA, 2014; MA *et al.*, 2013; PAJARES, 2015). In this sense, many multispectral and hyperspectral cameras have been developed, aiming small dimension, low weight, fast acquisition and good radiometric and spectral resolution to each application such as forest, agronomy, mining, and urban planning, for example (PAJARES, 2015).

Manea and Calin (2015) have proved that hyperspectral data depends strongly on the illumination conditions. Also, Honkavaara *et al.* (2009) states that the radiometric processing of UAV images is one of the most important steps, because the anisotropy of reflectance is influenced by illumination and atmospheric conditions. The reflectance factor is a function of the geometric structure of the scene and the solar angle besides the optical properties of the target which present sloped surfaces (KIMES, 1983).

One way of correcting illumination differences is by means of the Bidirectional Reflectance Distribution Function (BRDF), which considers two principal rays of light (one irradiated from sun to the surface, and another scattered from the surface to the sensor) (SHAEPMAN-STRUB *et al.*, 2009). Honkavaara *et al.* (2013) apply the BRDF correction in UAV acquired images for solar elevation angle of 43° to improve the image quality.

Another way is by correcting the micro and macro topographic effect, which can consider the topography of the scene or the target's structure, depending on the GSD, to identify the shadowed and illuminated faces of the target. The topographic correction is also known as illumination correction (SOLA *et al.*, 2013). It has been largely used in orbital images and many criteria-evaluations has been developed (BALTHAZAR *et al.*,2012; CAMPOS *et al.*, 2019). However, topographic correction applied in UAV acquired images lacks in literature. Jakob *et* *al.* (2017) applied topographic correction models in hyperspectral data acquired with UAV and had promising performance for sun elevation of 23°.

The illumination correction is of great interest, since the spectral response of an interest target can be misrepresented when it is shadowed, as shown in Imai *et al.* (2019) and may also affect the estimation of parameters from image, such as reported in Zhang *et al.* (2015).

Therefore, in this work we assessed data from Rikola camera in tropical latitudes, where sun elevation angles are higher than in high altitudes such in the northern hemisphere, in two distinct situations: first in a usual flight for forest investigation and second in a specific field campaign with viewing and sun angles specifically chosen.

In Section 7 of our work we investigated non-Nadir data acquired using a hyperspectral camera on board a UAV and the anisotropic behavior through the Anisotropy Index (ANIX) of four different targets: dry soil, wet soil, forest and sugar cane crop. Due to the small camera field of view and low flight height, results have shown that only small angles varying from 0° (Nadir) to <17° are available to be assessed, but which are not enough to properly analyze the target's BRFD. Also, the ANIX did not show any pattern for the targets and its random behavior leads to believe that corrections considering only variation of illumination caused by the geometry between light source and sensor would be enough.

In Section 7 and 8 we investigated models to correct illumination differences based on the structure of targets and the sun position, using the digital surface model of scene to obtain the slopes and aspect angles of 10cm and 3 cm GSD. For forest scenes (GSD of 10 cm), the correction resulted in images over-corrected in edges of targets, such as in transition areas between sugarcane crop and bare soil and in trees' canopies edges. For images of a special target of known slope and aspect angles (GSD of 3 cm), the corrected images show high improvement of image homogeneity between different angles, evidencing that topographic correction models have high performance in minimizing the variability caused by shadowed and lighted surfaces.

2. HYPOTHESIS

We conjecture that the correction of a target surface illuminating differences in hyperspectral UAV acquired images based on the structure of the target, is enough to attenuate illumination differences caused by the radiance anisotropy effects in images.

3. OBJECTIVES

This work aims to assess the use of topographic corrections to unify the reflectance factor of the same cover class. To achieve this, we aim to:

a) Study how anisotropy and BRDF behaves in conditions found in our common flight

b) Apply models of topographic correction in test images of notable wavelengths

c) Assess the improvement of different models in normalizing data of the same target in different slope and aspect angles.

4. BACKGROUND

4.1. Imaging using Unmanned Aerial Systems

UAV (Unmanned Aerial Vehicle), also called UAS (Unmanned Aerial Systems) or RPA (Remotely Piloted Aircraft), among others, was originated in military programs mainly because of risky missions or dirty work (WATTS, AMBROSIA; HINKLEY, 2012). The use of these platforms for mapping purposes started approximately in the year 2004, when publications in this field of knowledge started. Since the beginning until the year of 2013 the publications have more than tripled in the area. This shows the quick evolution of the use of UAVs in high resolution remote sensing (COLOMINA; MOLINA, 2014)

Performance in UAV remote sensing does not denote low quality data, on the contrary, data tend to be of high spatial resolution and collected with all sorts of imaging sensor, depending on the purpose (COLOMINA; MOLINA, 2014). UAV remote sensing is intended to be similar to orbital remote sensing, and, thus, the techniques applied to process and analyze acquired data are, usually very similar although the quality, availability and applications may be different because of UAV-acquired data characteristics like stability (mainly for light weight platforms) (COLOMINA; MOLINA, 2014; YAO, QIN; CHEN, 2019) and distance to the ground.

Studies regarding the geometric processing of UAV images have being performed by comparing software from computer vision and specific for UAV data software such as Matashape (AgisoftLLC, St. Petersburg, Russia) and Pix4Dmapper (Pix4D S.A. Prilly, Switzerland) and by developing or adapting existing techniques. Authors have achieved good results, particularly when generating orthophotos and Digital Surface Model (DSM) (GINI *et al.*, 2013). Photoscan and Pix4D software are widely used for UAV data for many applications, such as Forest in Nevalainen *et al.* (2017), Imangholiloo *et al.* (2019) and Viljanen *et al.* (2018) and for agriculture in Osco *et al.* (2019) and Imai *et al.* (2017). This kind of product generated from UAV data is possible because the high density of points obtained with Structure from Motion (SfM) algorithms, which generally follow the same workflow: calculate the camera locations and generate a sparse cloud, generate a dense cloud and using the dense cloud to build a georeferenced mesh. (TMUSIC *et al.*, 2020). Errors to the SfM products can come from low-quality images and can be minimized by a good plan of flight and correct distribution of ground control points (TMUSIC *et al.*, 2020).

4.2. Hyperspectral Images

The use of multi-spectral images in aerial and orbital platforms is traditional and comes from the sixties when it was developed the concept of the spectral distribution of energy of each pixel, instead of only using operations that enhanced image's properties (LANDGREBE, 1997). In the 80-decade started the acquisition of collects of hyperspectral images with image spectroscopy (PLAZA *et al.*, 2009).

What differentiates a hyperspectral image to a multi-spectral image is the continuous and narrow bands characteristic of hyperspectral images but not the total number of bands. In this sense, a sensor with 20 narrow (10nm) and contiguous bands can be considered hyperspectral, while a sensor made of 20 wide bands or noncontiguous will be considered multi-spectral (QI, INOUE; WIANGWANG, 2012). Therefore, it is important to understand that there is no difference in the spatial resolution either in multi or hyperspectral sensors, but only spectral resolution are different (GOVENDER, CHETTY; BULCOCK, 2007).

When using contiguous and narrow bands, it is possible to understand the response of each pixel in an almost continuous spectrum, what makes it possible to deeply analyze objects in the surface as they respond reflecting light, what does not happen in multi-spectral image, which lose some information both because of the gaps between bands (GOVENDER, CHETTY; BULCOCK, 2007) and integration within a wide band.

4.3. How energy reflects from different surfaces

In order to have remote sensed data, it is necessary to: i) have a source of energy, ii) the energy must cross some mean and reach the interest target, iii) the energy interacts with the material of the target, and iv) the energy reflected by the target is received in a sensor and processed afterwards to extract data from it (HONKAVAARA, 2008; SABINS, 2007). The science that studies this kind of energy, the Electromagnetic Radiation (ERM) is called Radiometry (JENSEN, 2011; SHAEPMAN-STRUB *et al.*, 2009).

By the radiation balance equation, it is stated that a radiant flux (ϕ [Watts]) that comes to a surface will be balanced by the radiant flux absorbed, transmitted and reflected, as seen in (1), depending on the wavelength λ (JENSEN, 2011).

$$\phi_{r\lambda} = \phi_{reflected\ \lambda} + \phi_{absorbed\ \lambda} + \phi_{transmitted\ \lambda} \tag{1}$$

The portion of EMR that will suffer each of these phenomena depends, among other things, on the composition of the surface. When the surface's profile is much smaller than the wavelength that surface is considered flat and, therefore, the reflection is called Specular (or mirror-like) and it means that the incident radiant flux will reflect almost completely in the same angle, opposite direction. Whereas, if the profile of the surface is rough and its size is fairly the same size of the wavelength, then this surface is considered diffuse, and so is its reflection. It means that the surface will reflect in all directions in anisotropic way. In this regard, there exists the Lambertian surface, defined by Lambert (1892), which is considered to reflect equally in all directions (JENSEN, 2011). These tree kinds of surfaces are shown in Figure 1.

Figure 1 Representation of a Specular, not-perfect Specular, Lambertain and Anisotropic surfaces.

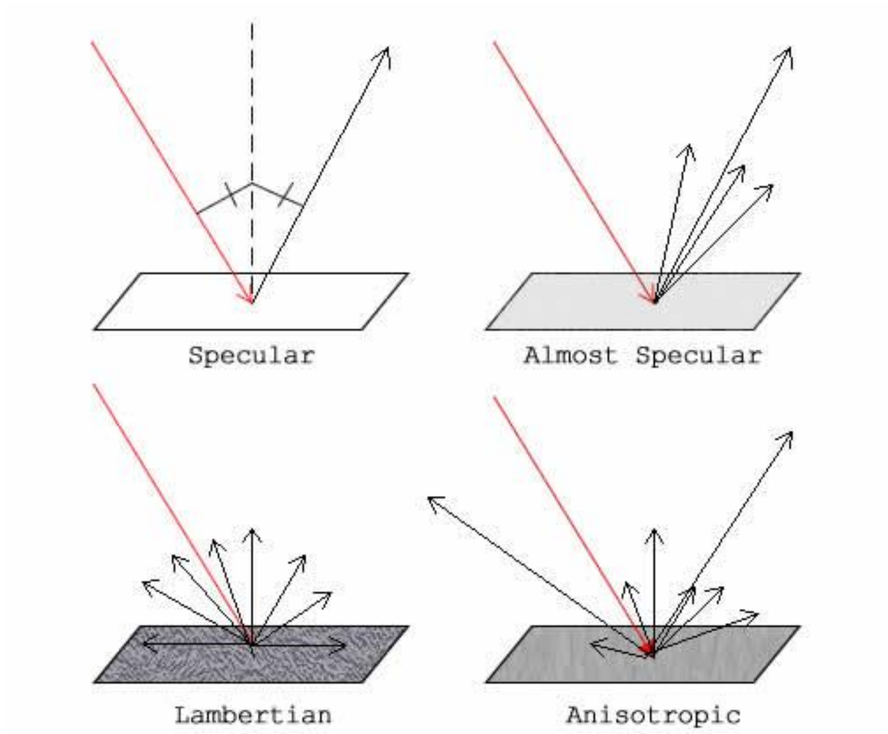

Source: Autor. Adapted from Jensen (2011).

Nicodemus *et al.* (1977) describes reflection as the process where the EMR incident on a stationary medium, leaves it without changes in its frequency. Reflectance, still, considers the incident flux as it is the fraction of incident flux that reflects. The incident flux and the reflected energy may assume three theoretical shapes: conical, hemispherical or directional. And combining these shapes it results in nine cases of reflectance quantities including only 4 measurable cases and 5 theoretical cases. The measurable ones are: biconical, hemispherical-conical, conical-hemispherical and bi-hemispherical. The theoretical quantities are: bidirectional, directional-conical, directional-hemispherical, conical-directional and hemispherical-directional (SHAEPMAN-STRUB *et al.*, 2009).

The most common case seen in literature is the Bidirectional reflectance distribution function (BRDF), which describes parallel beams of incident light to a surface and parallel beams of reflecting light into the hemisphere (SHAEPMAN-STRUB *et al.*, 2009). The BRDF is useful as a primary concept but cannot be measured because the elements of solid angles are infinitesimal and, so far, the radiant flux is not measurable. The function is expressed in (2). It is wavelength-dependent and relates the radiance reflected (Lr) and incident irradiance (Ei) (where r stands for reflected and i stands for incident) in a given wavelength (λ), zenith angle (θ) and azimuth angle (φ) (NICODEMUS *et al.*, 1977; SHAEPMAN-STRUB *et al.*, 2009).

$$BRDF_{\lambda} = f_r(\theta_i, \varphi_i; \theta_r, \varphi_r; \lambda) = \frac{dL_r(\theta_i, \varphi_i; \theta_r, \varphi_r; \lambda)}{dE_i(\theta_i, \varphi_i; \lambda)} \; [sr^{-1}] \quad (2)$$

To have actual values of reflectance, it is well known in literature the concept of reflectance factor. It was first stated by Nicodemus *et al.* (1977) and can also be modeled to 9 cases, considering the shape of light beans adopted. The basic one can be considered the biconical, which proposes a solid angle for both incidence and reflectance, as shown in figure 2.

Figure 2 Representation of the Bidirectional case of Reflectance

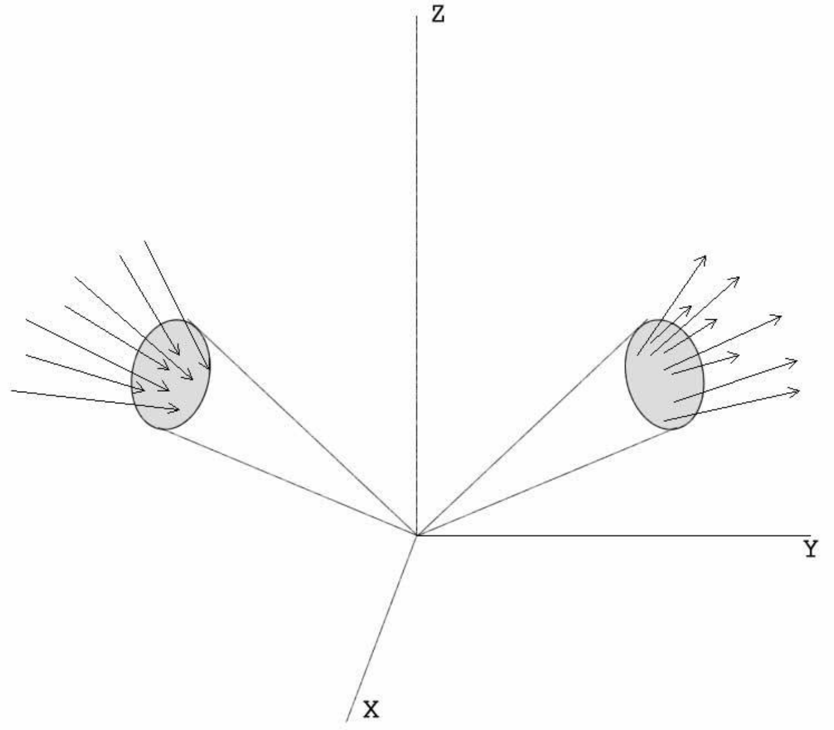

Source: Author. Adapted from Nicodemus (1977)

It is considered a factor because the reflectance is divided by the BRDF of a perfect (lossless) Lambertian (diffuse) standard surface. Another common way in literature to describe it is by the Bidirectional Reflectance Factor (BRF) which is given by the ratio of the two radiant fluxes, considering the same condition of irradiation. Equation (3) shows the BRF, dependent of the incident (*i*) and reflection (*r*) angles: θ zenithal and φ azimuthal, times π. The denominator is the reflection of a Lambertian surface, the reflection is equal regardless the angles and thus, its BRF can be expressed as its BRDF times π. Also because of the Lambertian property, the zenith and azimuth angles are omitted for an ideal surface (SHAEPMAN-STRUB *et al.*, 2009).

$$BRF_{\lambda} = \frac{f_r(\theta_i,\phi_i;\theta_r,\phi_r)}{f_r^{id}(\theta_i,\phi_i)} = \pi f_r(\theta_i,\phi_i;\theta_r,\phi_r)\ [dimensionless] \quad (3)$$

We see, therefore, that two concepts are fundamental to properly understand the characteristics of remote sensing data. One is how EMR is modeled and the geometry involved in obtaining data and the other is the way the surface interacts and reflects the EMR.

A classical approach of the reflectance model considers the target to be composed by many particles arranged in horizontal position, parallel and uniform but when studying other objects such as tree leaves in a forest canopy, for example, where the targets are unevenly distributed, it is necessary to take in to consideration the shadowing effects caused by the object's shape (LI; STRAHLER, 1992). Civco (1989) also points out that the spectral variability caused by shadowing of surfaces which are not normal to the source of irradiance is artificial, in a sense that it can't be considered part of the spectral variability of a particular cover class. That is the main concern behind the topographic correction.

4.4. Topographic correction

Initially, the effects of topography caused in images, were considered undesirable mainly because of the disturbance caused in classifications results (M. TEILLET, GUINDON; GOODENOUGH, 1982). Thus, in early developments of Landsat MSS, topographic correction procedures were developed based on the geometric properties of topographic effect (M. TEILLET, GUINDON; GOODENOUGH, 1982).

The variability of spectral response for the same cover class is intrinsic but it can be steep when caused by a variation in slope and aspect and so is to be considered artificial because illumination of and radiance from features on a plane not normal to the source of EMR does not represent the spectral response of that feature. This effect is amplified in low sun angles condition and in areas with large topographic effects (CIVCO, 1989).

Many models have been developed to correct topographic effects in images, mainly focusing on orbital multispectral sensors. The ones to be used in this work are described below. In most cases it is necessary to model firstly the conditions of illumination (IL), represented by the cosine of the illumination (cos(i)), as shown in equation (4). This model is based on the cosine law for spherical trigonometry and was proposed by Sellers (1972). It relates the solar zenith (θ_0) and azimuth (ϕ_0) angles, aspect (ϕ_n) and slope (θ_n) of the terrain (M. TEILLET, GUINDON and GOODENOUGH, 1982).

$$IL = \cos(i) = \ cos\theta_0 cos\theta_n + \ sin\theta_0 sin\theta_n \cos{(\phi_0 - \phi_n)} \qquad (4)$$

Two vectors are important to define properly terrain's aspect and slope. One is the the Normal, a vector which is perpendicular to the surface, and is calculated by the vector product of two vectors in the surface, being these vectors defined by two points each, having one point in common. Nadir is the vector pointing directly to the Earth's center of mass at a given location. Thus, we define aspect and slope.

The terrain's aspect is calculated by the azimuth angle of the Normal vector, which is calculated between the position to where the terrain is facing and the North clock-wise counting. Thus, it can vary between 0º to 360º. We define the slope as the angle of declivity of the surface in degrees ranging from 0° to 90°, measured between the Nadir vector and the Normal vector to the surface. Both are generated from a DSM. Figure 3 illustrates the aspect and slope angles.

Figure 3 Representation of aspect and slope angles

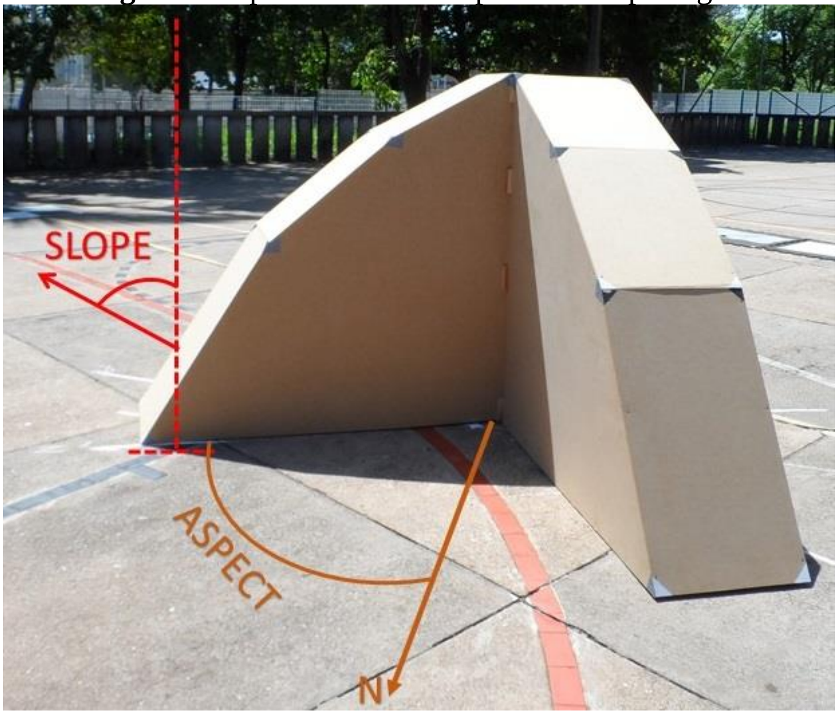

Source: Author

The most simply way to correct topographic effects is called the cosine correction. It was broadly used to illumination transformations in satellite data when assuming a flat terrain. Its corrected factor (L_C) is obtained by multiplying the value obtained in the image (L_0) and the product of the cosine of the solar zenith angle (θ_0) by the cosine of illumination (cos(i)) (equation 5) (M. TEILLET, GUINDON; GOODENOUGH, 1982)

$$L_C = L_0 \frac{\cos(\theta_0)}{\cos(i)} \quad (5)$$

Also, as proposed by Smith et al (1980), the simple ratio between the value obtained in the image (L_0) and the cosine of illumination (cos(i)) is a way of minimizing effects of directional scattering in mountainous terrain, using a Lambertian approach. This assumption is more valid for slopes of less than 25º and illumination angles of less than 45º. This is shown in equation 6.

$$L_C = \frac{L_0}{\cos(i)} \tag{6}$$

M. Teillet *et al.* (1982) also proposes another function called semi-empirical cosine. This is expressed in equation 7. It adds a constant called C, obtained dividing “A/M”, being A and M coefficients in the linear regression L=A+M *IL, where L is the reflectance of a known corrected target.

$$L_C = L_0 \frac{\cos(\theta_0)+C}{\cos(i)+C} \tag{7}$$

Civco (1989) proposed a model to obtain topographically normalized images, by using the mean value of illumination (ILm) in the equation, showed as equation 8.

$$L_C = L_0 \frac{ILm-IL}{ILm} \tag{8}$$

All models cited before consider the surface to be Lambertian even though this assumption is more likely to be true for slopes less than 25° and illumination (IL) angles of less than 45° (M. TEILLET, GUINDON and GOODENOUGH, 1982).

Jakob *et al* (2017) suggests that it is also possible to use topographic correction in UAV acquired data, and shows good results to more homogeneous surfaces.

5. PERFORMED TESTS

In this part of the dissertation, we describe the performed experiments, acquired data and respective analysis. It is divided in three main topics: first, in chapter 6, we present the tools required for data acquisition such as camera, platform and other. Then, in chapter 7 we present a first set of experiments using field data in a forest area and in chapter 8 we present a second set of experiments, performed in controlled environment using a specific target to study the behavior of topographic correction models in different angles.

6. SENSORS AND ACQUISITION PLATFORMS

To acquire images, we used the UX4 UAV, developed by NuvemUAV. It has 4 propellers and a battery that allows up to 30 minutes of flight. The UAV carried two cameras, a Rikola Hyperspectral Camera (Senop Ltd), as shown in Figure 4, and a Gopro Hero 4 (Gopro Ltd.).

Figure 4 Rikola Hyperspectral Camera produced by Senop Ltda

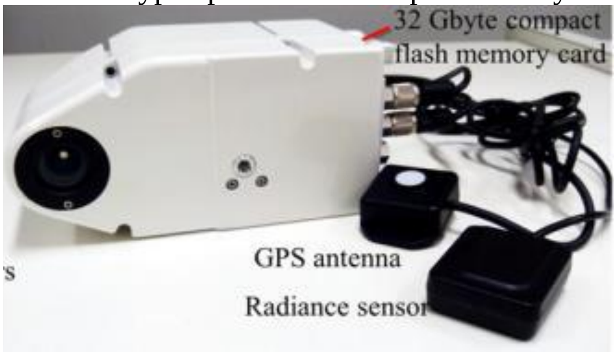

Source: Oliveira (2016)

Figure 5 UX4 UAV

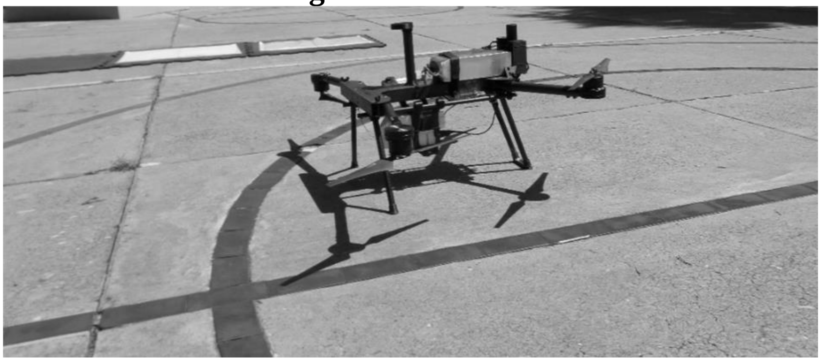

Source: Author

The Rikola frame camera (showed in Figure 4) is composed by two frame sensors, a Fabry-Pérot Interferometer (FPI) and a beam-splitting optics (OLIVEIRA; TOMMASELLI; HONKAVAARA, 2016; BERVEGLIERI; TOMMASELLI, 2016). The operation of its interferometer allows flexibility of bands configuration (MIYOSHI, 2016). An FPI device is composed by two semi-reflexive mirrors to acquire different wavelengths using a gap between two mirrors and its reflective properties. Also, the camera has two sensors for which the beam splitting optics directs the wavelengths (BERVEGLIERI; TOMMASELLI, 2016; HONKAVAARA, *et al.*,2013). The operation of an FPI is shown in Figure 6.

Figure 6 Operation of the FPI in Rikola Camera, where transmitted beams are read in Sensor 1 and reflected beams are read in Sensor 2 after being selected by the FPI.

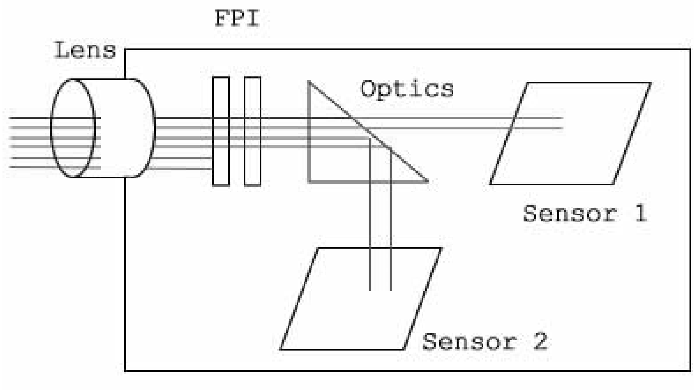

Source: Adapted from Oliveira (2016)

A frame sensor acquires the whole scene at the same time, unlike scanning sensors such as whisk-broom or push-broom (AASEN *et al.*, 2015). Because of this characteristic, it is possible to obtain overlap areas between consecutive images and in-flight lines, which allow obtaining parallax and also stereoscopy analysis (JENSEN, 2011). Besides that, it is also feasible to have multiple viewing angles (ROOSJEN *et al.*, 2017).

Rikola Camera (model DT-0011) can acquire up to 50 bands in a set of bands from near locations, here called photogrammetric cube. Since it acquires one band per time in each sensor, there is a delay between the images so when taking images using a UAV there is a small displacement between each spectral image band, which must be taken into consideration in the image processing step (OLIVEIRA, 2017).

The minimum spectral resolution of Rikola's sensor is 10 nm, measured by its Full Width at Half Maximum (FWHM), the width (in nanometers) of the sensibility curve of the sensor measured in the half height of the curve's peak (BORENGASSER, HUNGANTE; WATKINS, 2007).

The advantages of this camera are: the sensor is frame-type, low weight (approximately 700 g), high spatial resolution when carried by UAV (within centimeters), flexibility of bands configuration and narrow bands that guarantees hyperspectral data (MIYOSHI, 2016). A summary of Rikola's characteristics is presented in Table 1. This camera has been used in several applications of remote sensing such as citrus harvest (MORIYA *et al.*, 2019), forest (MIYOSHI *et al.*, 2018), agriculture (IVUSHKIN *et al.*, 2019) and mineral exploration (JAKOB *et al.*, 2017) among others.

Table 1 Rikola Camera charactheristics

Weight	720 g
Size	77mm x 89.5mm x 152mm
FOV	36.5
Number of bands	25
Sensor	CMOS model CMV400
Focal	9mm
Image dimension	1010 pixel x 648 pixel
Pixel Size	0.0055 mm

Source: Author

Honkavara *et al* (2013) suggests that the processing of data cubes from the FPI data requires correcting spectrally the images, corregistering the bands and orientating each frame to obtain accurate data because of the small displacement between the spectral bands of the photogrammetric cube. For more details see HONKAVAARA (2013).

Also, to be able to obtain the reflectance value of the targets and know the incidence of solar radiation during the field campaign, we used a spectrometer. The Spectrometer (model is FieldSpec HandHeld ASD - Malvern Panalytical ltd) collects data from 325 nm to 1075 nm. It has a Field of View (FOV) of 25° but can be reduced to 10° or 1° by using lens from the sensor. In this work the FOV was set to 1° to guarantee minimum interference from adjacencies. Data was collected from interest targets, as described in the following section, and also the sun irradiance was collected in the cosine mode. The spectrometer was placed in a separated area which didn't have shadow interference, as shown in Figure 7. We used a device to hold it perpendicular to the ground, and measurements were made during each flight time.

Figure 7 Operation of the spectrometer to acquire irradiance data.

Source: Author

7. PRELIMINARY TESTS WITH RIKOLA CAMERA

7.1. Context

These tests are based in the fact that the anisotropy of one target is different from another, causing light to reflect in different proportions depending on the viewing angle and the characteristics of the target, such as its composition and structure. In this way, anisotropy could be used as a parameter to distinguish different targets with very similar spectral response. To assess the influence of anisotropy in our targets, we used one radiometric cube with 25 bands and analyzed the spectral response in all viewing angles from a UAV flight. Two tests were made: the first one to see the different view angles available in a common UAV flight using Rikola camera and the second one to analyze the anisotropy index behavior in different targets for all the view angles available.

We also applied 3 models of topographic correction in this cube to assess its performance in attenuating the lighting differences caused by shadowed and lighted areas.

7.2. Data acquisition

To guarantee a consistent analysis of the behavior of anisotropy in different targets, we chose an area with as many cover classes as possible in our database. The area is located in south-west part of São Paulo state, Brazil. There is an Atlantic Forest remnant located in the area, part of an Ecological Station called “Mico Leão Preto”. Its location is depicted in Figure 8.

Figure 8 Location of the Study Area in south-west of São Paulo state, Brazil

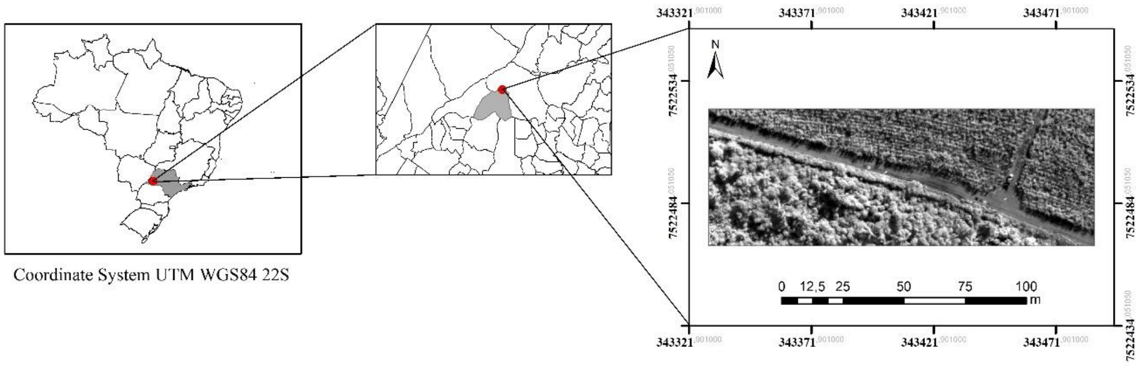

Source: Author

Within this test area it is possible to find dry soil, wet soil, sugar cane crop and forest, as can be seen in Figure 9. Besides the heterogeneity of the area, it is of great importance to researches currently being developed regarding the targets found there.

Figure 9 Interest targets found in the study area, highlighted the key color and texture for each.

(1) (2) (3) (4)

Sugar cane crop | Dry soil | Wet soil | Forest

Source: Author

The bands chosen to be used in this study range from green to near-infrared, as shown in Figure 10. The UAV flights height (above ground) was approximately 160 m with 4 m/s of velocity. This flight produced images with a GSD (ground sample distance) of about 10 cm. The flights were performed in July 1st, 2017 at 10:00 am (UTC -3) in a cloudless sky and at minimum wind possible (wind gusts less than 5 m/s). The Sun Zenith angle was 31.12° and Sun azimuth angle 41.98°

Figure 10 Configuration of Rikola Camera. In bars are the wavelengths of the 25 bands and in line is the FWHM for each band

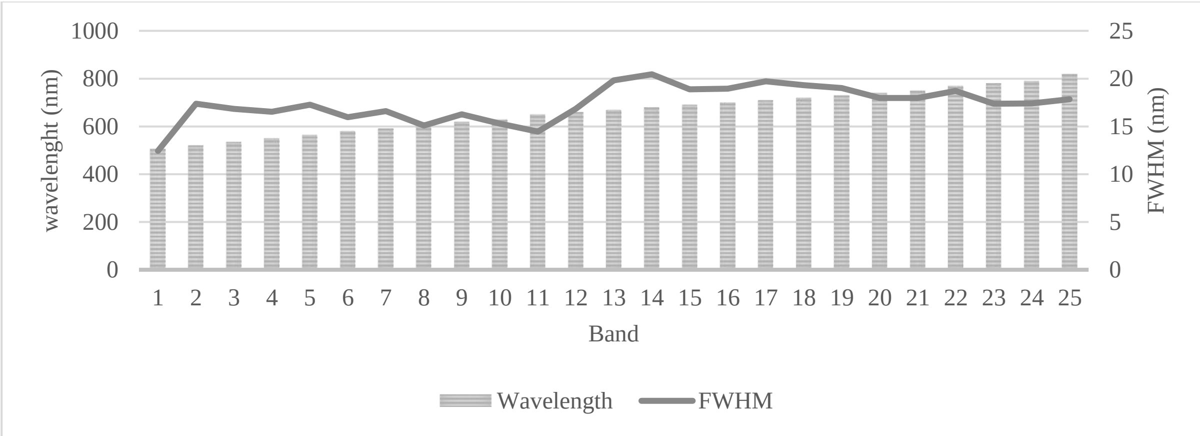

Source: author

For this acquisition there were tree flight lines, one parallel to the road visible in the area and two perpendicular to the road, towards and from the inside of the forest, as a transect to explore this target. This can be seen in Figure 11.

Figure 11 Position and Direction of the flight lines for image acquisition. One (1) parallel to the road and two (2 and 3) perpendicular

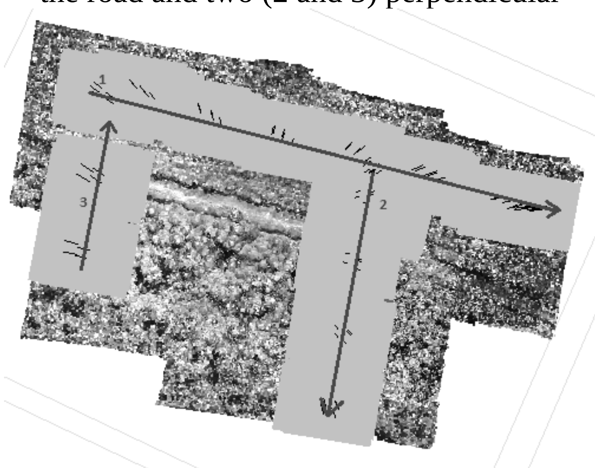

Source: Author

After acquiring the images, some steps were followed to obtain orthorectified images, DSM and reflectance images in an adjusted block. All the steps are described in the following and represented in Figure 12.

The first step is to correct the dark current from the images, a standard procedure for this camera that removes noise caused by electronic current. Data was then transformed to TIFF format file and all the pictures taken in one campaign must be processed in a software such as PhotoScan to compute their positions and orientation. In this process, 4 bands are used as reference; two from each camera sensor as recommended by previous works such as Honkavaara *et al.* (2013). This is needed to guarantee the compensation of the displacement between the sensors. From the block formed, two products are obtained: one sparse point cloud to be used in the radiometric adjustment and one regular grid of 10 m distance between points. This grid is what dictates the points that will be used to compute the viewing/lighting geometries used to the radiometric correction in sequence. To have more detailed data from different view angles, another grid of 0.5 m was crated and processed.

Figure 12 Flow chart of all the steps involved in this work

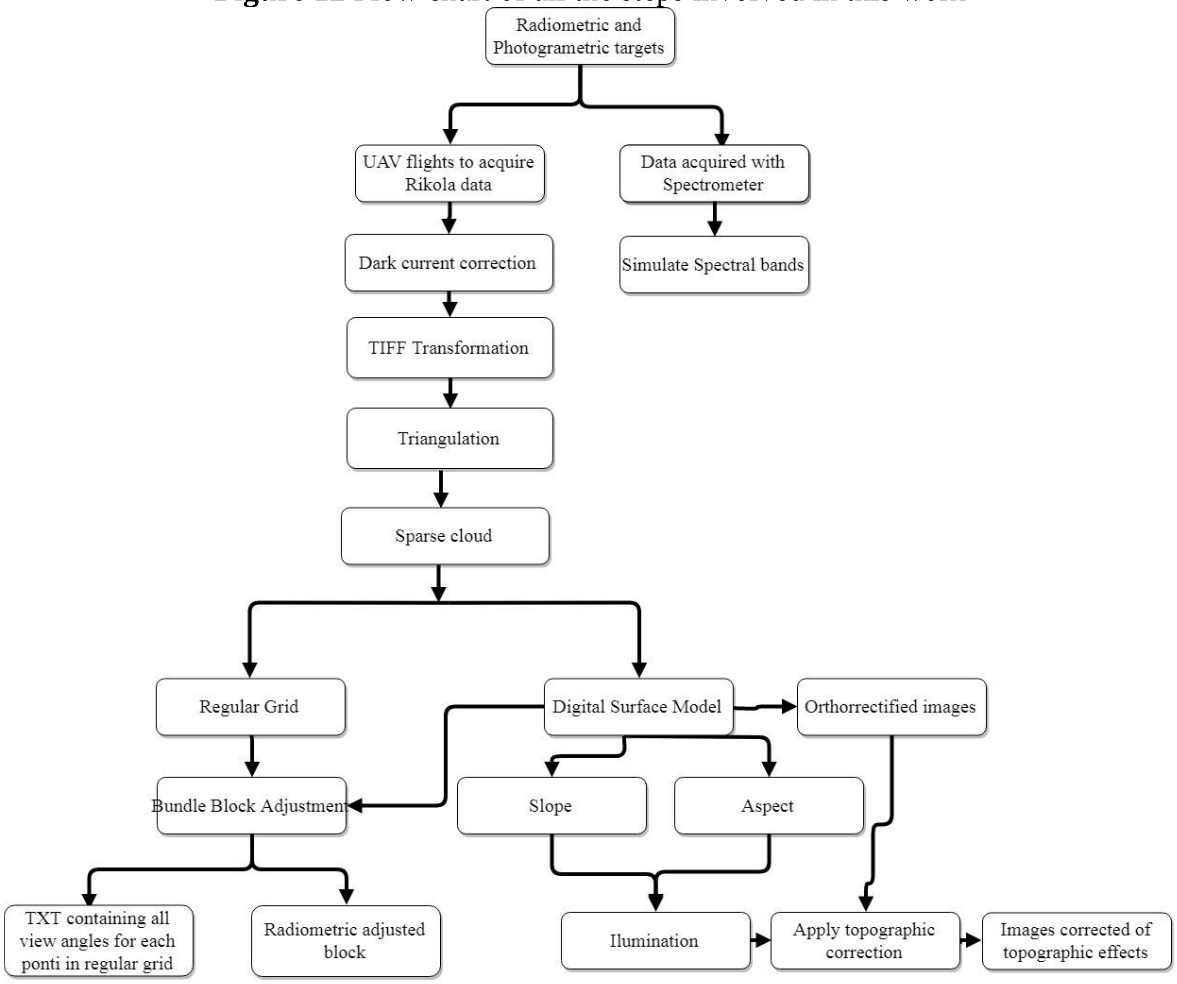

Source: Author

After that, the images were submitted to a radiometric adjustment, which corrects the BRDF and its resulting variation in illumination and also variations caused by the movement of sensor regarding the sun position. This is done by finding homologue points in image from a regular grid produced from the photogrammetric triangulation (HONKAVAARA *et al.*, 2013). In this process one of the byproducts is an TXT file that contains, for each point of the regular grid, the image that contains the point, the viewing angles and the digital number (DN) of the pixel. All these radiometric procedures are done by a private software developed by the Finnish Geospatial Research Institute.

To obtain the value of reflectance factor, the DN values were interpolated by the empirical line, which uses the reflectance factor of radiometric panels to obtain physical measurements of the acquired scene. This transformation is based on the stated by Smith and Milton (1999) that is described next. The empirical line method requires that some targets are inserted in the flight to appear in the images and their reflectance is measured by a field spectrometer because it can acquire more spectral information of targets. Data from the spectrometer is transformed to reflectance factor and estimated for the image bands of the sensor used. When using at least two targets, one dark and one light, it is possible to estimate parameters that relates, to each wavelength, the radiance recorded by the sensor and the reflectance measured by the spectrometer. In a graphic (here represented in Figure 13), the reflectance versus radiance response is drawn in a linear relationship, and generates a transformation equation which can be applied to the entire scene, regarding each wavelength (SMITH; MILTON, 1999)

Figure 13 Scheme of how the transformation is made from radiance to reflectance

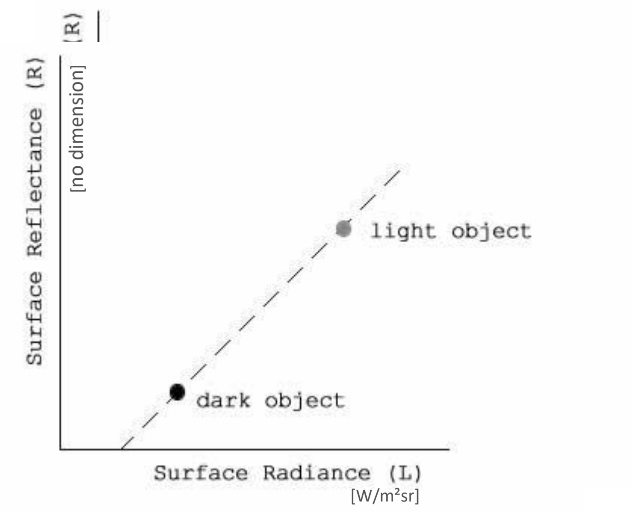

Source: Author. Adapted from Smith and Milton (1999).

7.3. Initial Experiments

In the following section the preliminary experiments are described along with the results which made possible to properly outline the research. Three experiments were done, the first one investigates the viewing geometries of four targets in the interest area, showing how Rikola camera can be used as a tool to acquire data in other viewing angles rather than nadir position. The second trial assesses how the viewing geometries affect the reflectance anisotropy of targets. The third experiment is an initial test of the behavior of topographic corrections applied in our hyperspectral images, highlighting the positive aspects and the improvement needs.

7.4. The view geometry of Rikola sensor

This first experiment intends to understand the geometry of each pixel and how this information can be used to study light behavior in different land cover. To achieve that, Honkavara's software was used to identify for each point in a regular grid of 0.5 m x 0.5 m the images in which this point appeared, the zenithal and azimuthal angles and the digital number (DN) of that pixel acquisition geometry (HONKAVAARA *et al.*, 2013).

Squared samples with 50 pixels x 50 pixels were extracted from each land cover. The files obtained included the view angles for all images where the points appeared, as explained before (section 7.2). In this way we could analyze the variance in the viewing angles of all images which contained the points inside the interest area. In Figure 14 is possible to see each of the sample areas identified.

Figure 14 Targets used in preliminary tests from this work, squares of 50 x 50 px from each land cover encountered

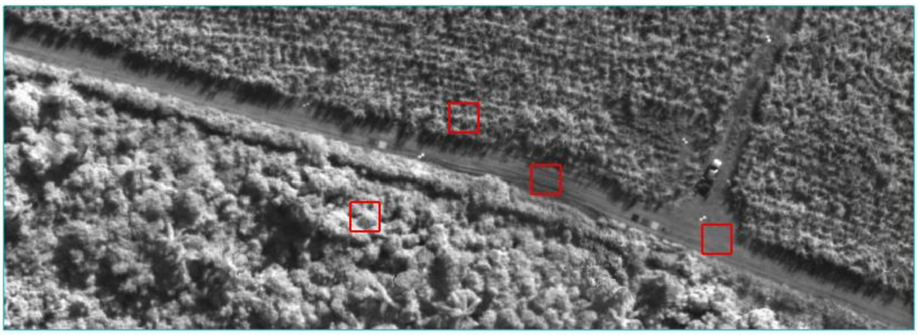

Source: Author

As a result, is possible to plot as in Figure 15 the distribution of the angles in each specific square. Because of the configuration of flight lines, the azimuthal angles are larger in forest target (which is covered by the four flight lines) and thus the azimuths of the viewing angles range in almost all directions. On the other hand, points imaged by only one flight line lack of azimuthal views in most directions, having data mostly in forward and backwards direction of the flight line.

Concerning the zenith viewing angle, it ranges from 0° to approximately 15°, being 0° the nadir view. In most cases, the angles vary in lower values (less than 10°). The reason for this small variation in zenith angles is because of the sensor's Field of View (FOV) and the forward overlap used of 60%.

The azimuth angle, however, have much smaller variability because of the flight lines. Thus, the angles are mostly oriented in directions forward and backwards the flight line direction. It is important to notice that even though the representations in graphics are for all 25 bands, analysis concerning any kind of view/reflecting geometry are wavelength dependent.

Figure 15 Viewing angles of each land cover for 25 bands of Rikola Camera. The concentric circles represent the zenith angle and the direction is the azimuth angle

(1)

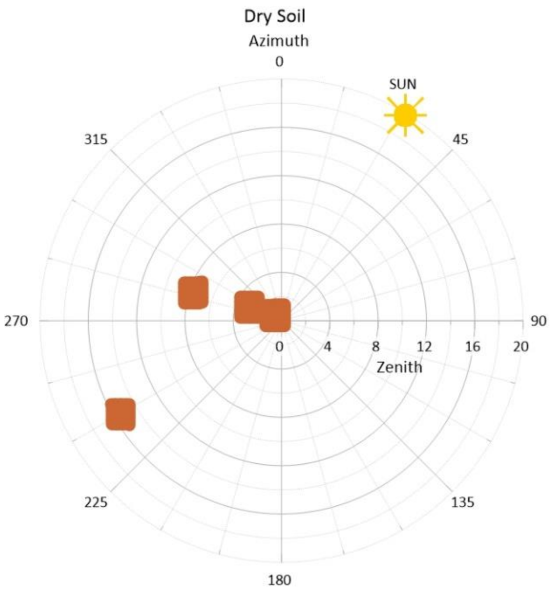

(2)

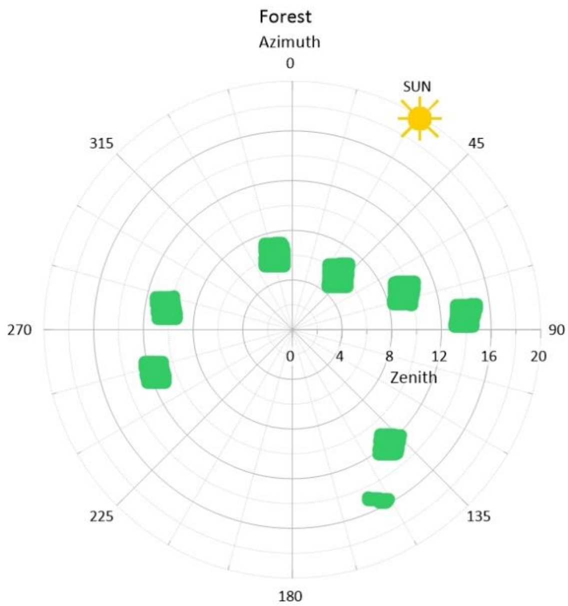

(3)

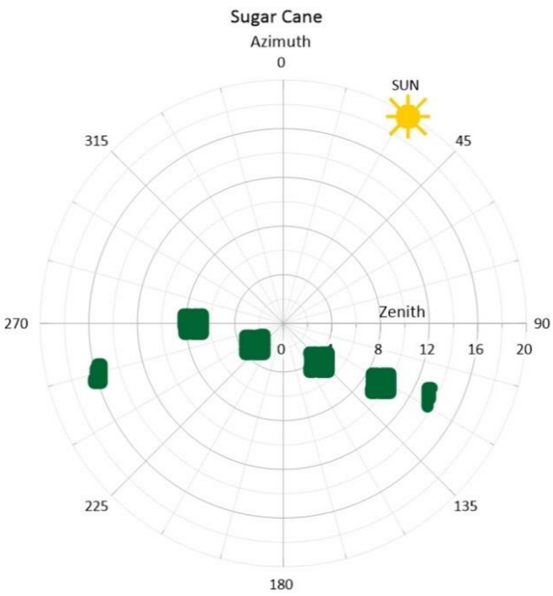

(4)

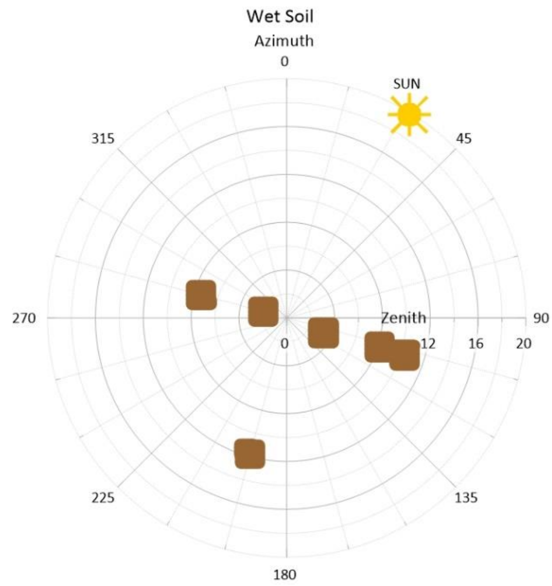

Source: Author

As mentioned before, what is influencing the viewing geometry of the flights are the camera geometry and flight characteristics. The FOV of 36.5° for a flight height of 160 m entails a real area covered of 105.52m in the flight line. Since there exists a delay between the band acquisitions, the maximum displacement between bands would be for bands 1 and 25. The time between these two shoots is 0.779s, what results in a displacement of 3.116m. This is illustrated in Figure 16. Considering the imaged line of 105.52m, this displacement is scanty in terms of variability of viewing geometries. In other words, in Figure 15, the points clustered are caused by the repetition of geometry in the 25 bands and the slight variation is caused by this displacement from the first and last bands.

Figure 16 Changes in the viewing angles between the first and last bands (without scales)

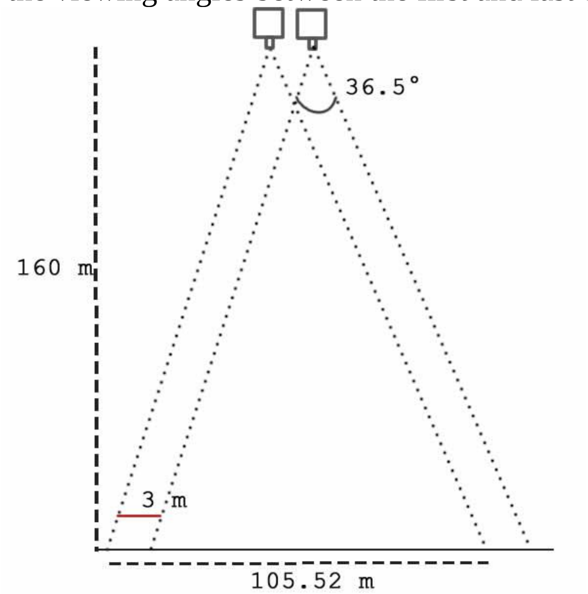

Source: Author

7.5.How changes in geometry affect anisotropy of targets

As said before, anisotropy is the characteristic of non-equal reflection of energy by targets depending on the direction (Jensen, 2011). Indeed, it is expected that targets with the same chemical and physical structure have the same variation in anisotropy when changes in view-illumination geometry occur. It is stated by many authors and thus it is necessary to know about our targets, the variation anisotropy can cause in the conditions of variation explained in item 7.4 (KOUKAL; ATZBERGER, 2012; MORIYA, IMAI; TOMMASELLI, 2018; ROOSJEN *et al.*, 2017).

In this sense, the second analysis performed in our data was an assessment of the anisotropy variation of the same targets in one reference band. The band randomly chosen was the green band (535.09 nm). Two ways of analyzing anisotropy are proposed as follows.

Sandmeier *et al* (1998) proposes to normalize the reflectance factor of a target to the signature of that respective target, measured in the nadir position as a way of measuring the target anisotropy. This value is dimensionless and is called by the authors the ANIF (Anisotropy Factor). It relates the energy reflected *(R)* in a specific direction of zenith angle (θ) and azimuth angle (φ) by the target and the reflectance in the nadir (R_0) where the index *i* stands for incident and *r* stands for reflected for a given wavelength (λ). The ANIF is showed in equation 9.

$$ANIF = \frac{R\ (\lambda, \theta_i, \varphi_i \theta_r, \varphi_r)}{R_0(\lambda, \theta_i, \varphi_i)} \tag{9}$$

Still, it is proposed to use the Anisotropy Index (ANIX). This ratio showed in equation 10 evolves the maximum (R_{max}) and minimum (R_{min}) reflectance factor of an interest target in a given view azimuth and zenith angles and given wavelength (λ). ANIX is more related to structural properties of the target (SANDMEIER *et al.*, 1998).

$$ANIX = \frac{R_{max}\ (\lambda)}{R_{min}(\lambda)} \tag{10}$$

Sandmeier *et al*. (1998) states that the anisotropy of a target occurs in all wavelengths, varying according to the physical and chemical characteristic of the material, similar to its reflectance signature. So, as trial basis we run tests in only one band (3-green, 535.09 nm), calculating the ANIF. Results are represented as 3-D plots in Figure 17.

Figure 17 3D plot of Anisotropy Factor (ANIF) for dry soil, Forest, Wet Soil and Sugar Cane Crop when varying azimuth and zenith view angles

(1) (2)

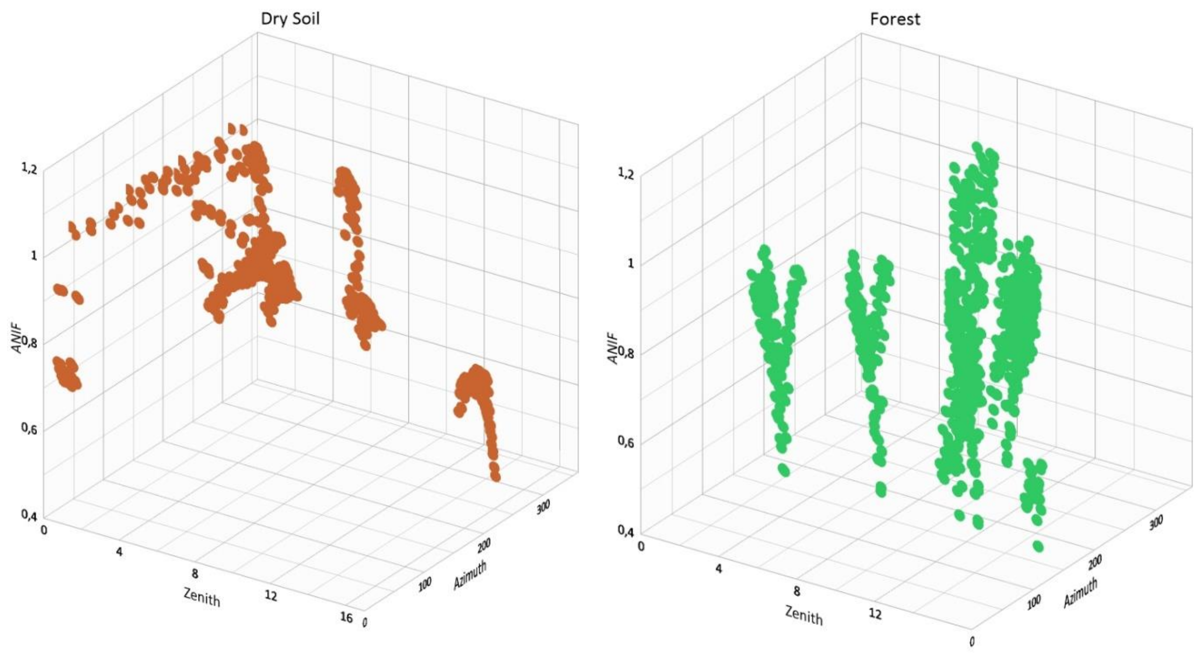

(3)

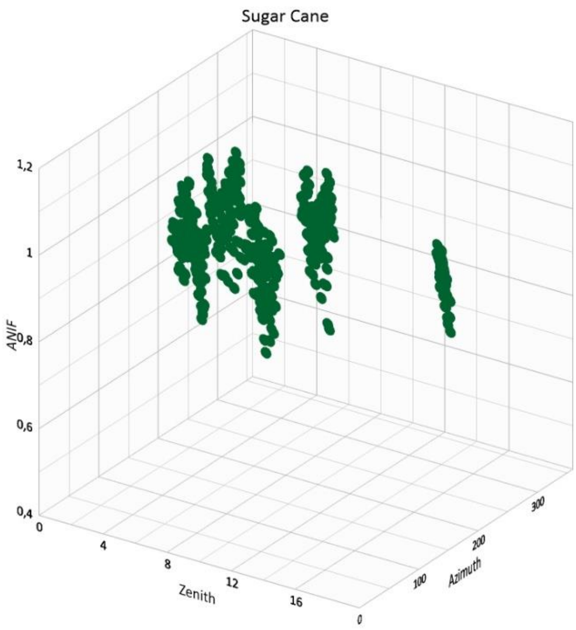

(4)

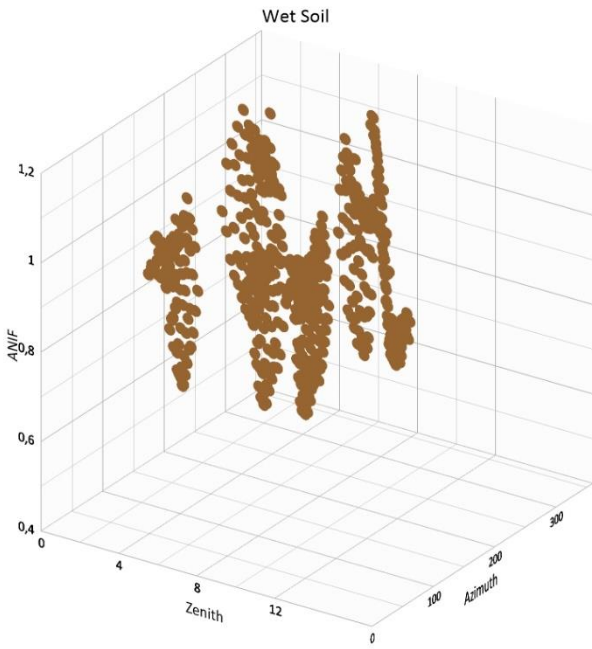

The results for ANIF show that no pattern can be found when comparing the four targets of this study. Although the target Dry Soil looks a little bit different, it cannot be directly associated with the target itself, but it can be a result of the different pattern of the viewing geometry of this target. In most cases, even when the azimuthal and zenithal angles vary (Z and X, respectively), the ANIF varies equally, making it impossible to properly differentiate the target by its anisotropy factor.

On the other hand, the anisotropy index (ANIX) is calculated for a given azimuth and zenith angle. In a quick analysis of figure 13, it is easy to notice that not all targets have a common viewing geometry in which it should be feasible to compare the ANIX for all 4 of them. It means that a great obstacle in analyzing this kind of data acquired in regular UAV flight is the comparability of data. It is, indeed, possible to calculate ANIF and ANIX for each target, but not in a comparable way.

A solution would be a planned acquisition to obtain the same viewing geometries for all interest targets, with great variability, at least ranging from 0° to 40° degrees in zenithal angle, as is proposed in related works as Grenzdörffer and Niemeyer (2012) and Roosjen (2016).

As a conclusion, it is possible to acknowledge that in usual flights such the ones performed regularly in our field surveys, the influence of anisotropy is regular in all bands and does not vary in significantly because the changes in viewing angles are small.

7.6. On the topographic correction models applied in Rikola Camera images

Some of the models described before were tested in this same database, to check how the wavelengths and targets of our proposed area would behave. The first step was to calculate the cosine of illumination IL as an image, using data from Sun position and a DSM obtained with Photoscan software. Then, one by one the models were applied. The equations used are specified in Table 2.

Table 2 Models of Topographic correction applied in this preliminary test

Model	Reference	Equation	Author
MOD1	Simple Ratio	$L_C = \frac{L_0}{IL}$	Smith et al (1980)
MOD2	Cosine	$L_C = L_0 \frac{\cos(\theta_0)}{IL}$	M. Teillet; Guindon; Goodenough, (1982)
MOD3	Normalized	$L_C = L_0 \frac{ILm - IL}{ILm}$	Civco (1989)

Source: Author

Models were applied in two bands, number 3 and 22 (green and Infra-Red (IR)), aiming to check the performance in both camera sensors, both bands were chosen randomly. Results are shown below and is possible to see that none of the models performed equally in the entire scene.

The MOD1, a simple ratio between the cosine of illumination (IL) and the DN was applied and it results are presented in Figure 18. Even being the simplest analyzed model, its result looks very alike MOD2, which considers the sun angle in the equations.

Figure 18 MOD1: Simple Ratio Model applied in bands b (a) and 22 (b)

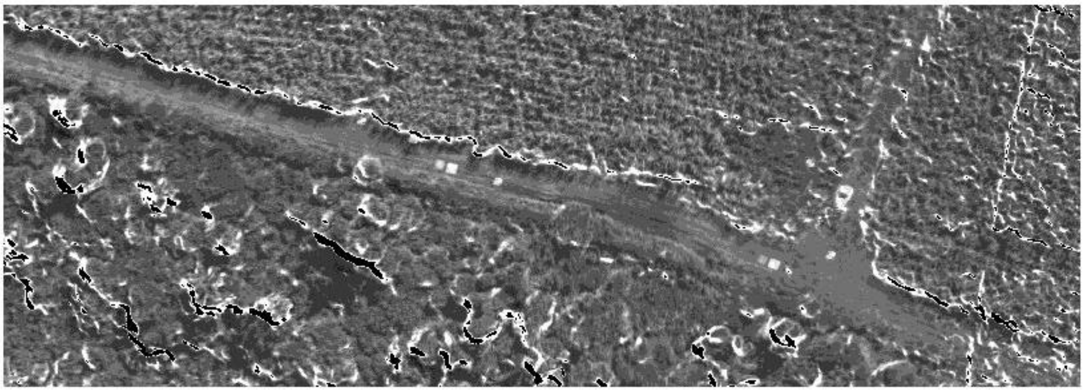

(a)

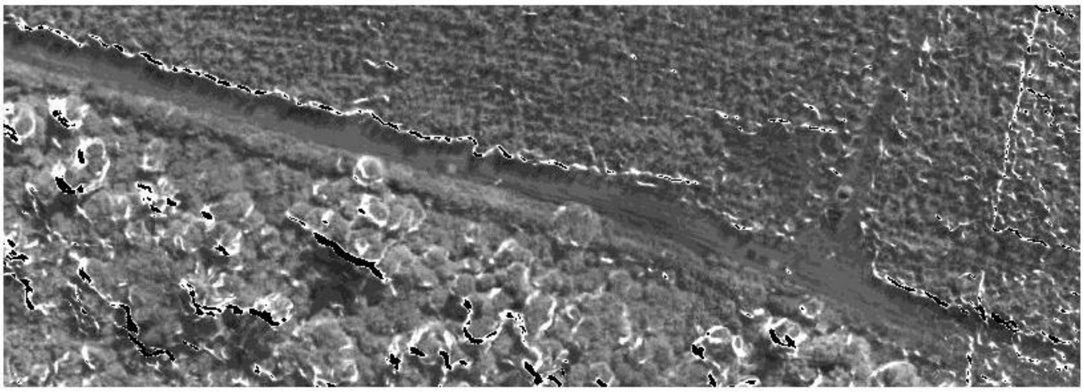

(b)

Source: Author

.

The MOD2, applied to bands 3 and 22 is presented next. The darker values are negative ones, result of the model. For some canopies in the forest area is possible to see a better homogeneous area for the two bands, but in the borders the correction applied evidence overcorrection, since the pixels get too bright or completely black. These results are displayed in Figure19.

Figure 19 MOD2, cosine model, applied to band 3 (a) and band 22 (b)

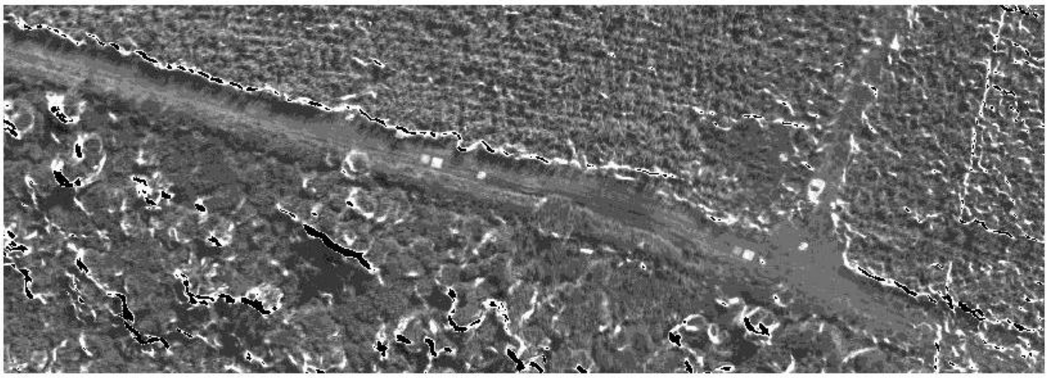

(a)

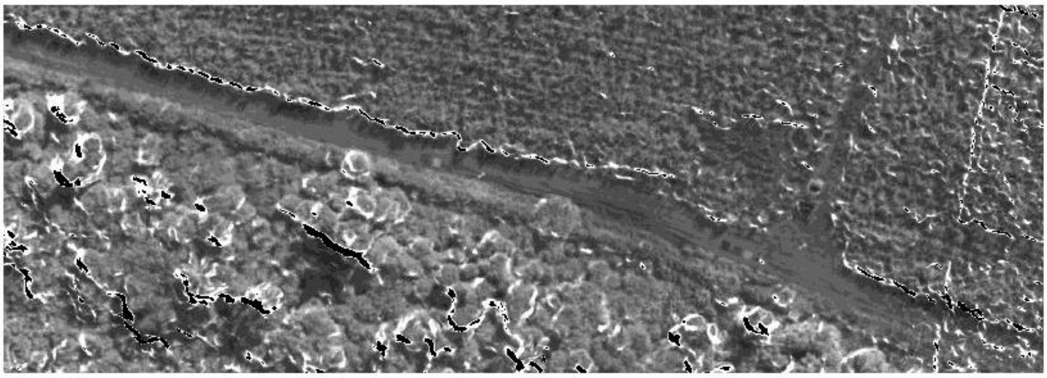

(b)

The results with the MOD3, are shown in Figure 20. The correction in both bands make all pixels look bright and the texture information is lost in many targets. In this case, the borders seem to be smoother and pixels do not get bright in excess, although they are still too dark in some points. The model seems to consider shadowed targets without reflection, and therefore, no data. Thus, the correction in these targets results in loss of information. Further investigation about this model limitation is not possible due to the uncertainty caused by the used DSM.

Figure 20 MOD3, Normalized, applied to band 3 (a) and band 22(b)

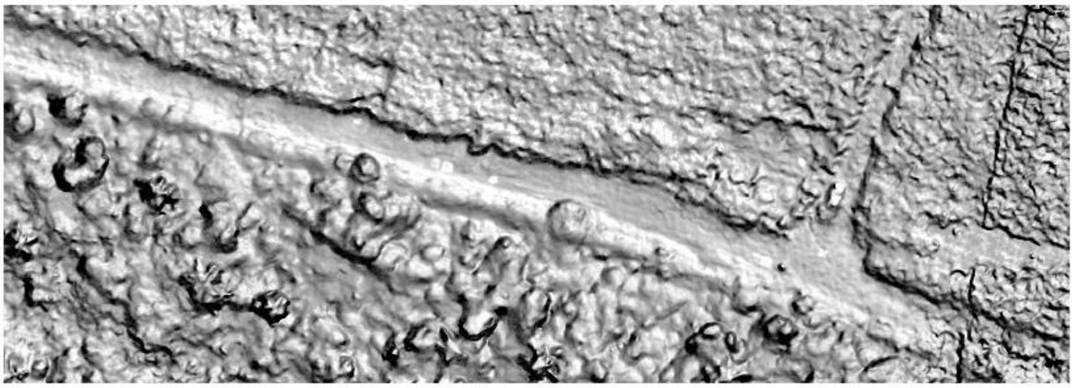

(a)

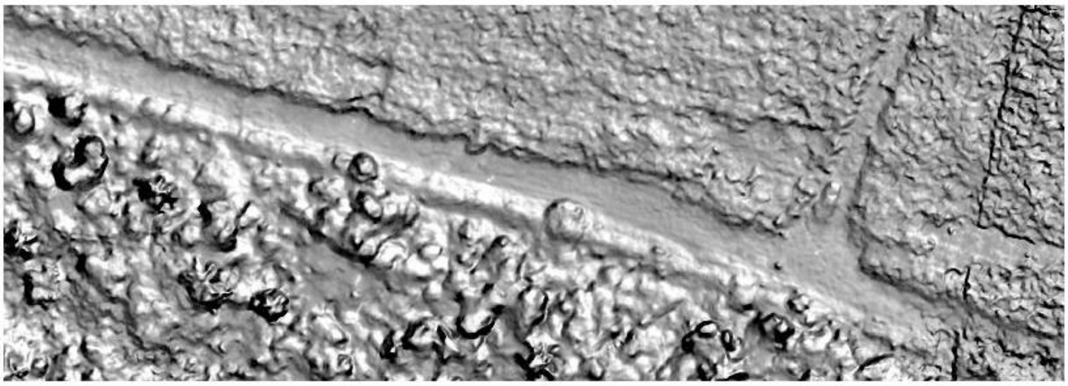
(b)

Source: Author

7.7. Partial Analysis

In this chapter we first assessed the performance of Rikola camera in regular UAV flights to provide data with non-Nadir viewing angles. Our results demonstrated that in that conditions the lack of data didn’t enable significant analysis of dependence of the reflectance factor with respect to the viewing angle.

Moreover, we analyzed the anisotropy of our data by means of the ANIX and concluded that the anisotropy factor had random behavior for the four tested targets (dry soil, wet soil, forest and sugar cane). These results lead to believe that the illumination correction, also known as topographic correction would be enough to correct the variability of reflectance factor among targets for that specific case.

Thus, we applied three topographic correction models in our forest images. The results evidenced promising results, although in transition areas, where the terrain slope is sharper, the outcome was not satisfactory.

We notice different performance in the models and although the promising result, the high complexity of surfaces and the unknown amount of DSM contribution in the model performance it is impracticable to further analyze the results.

In this sense, from these results, there was a need to investigate which parameters of the topographic correction models were responsible to the overcorrection in targets edges. Thus, we performed some controlled experiment described in section 8.

8. ASSESSING THE BEHAVIOUR OF TOPOGRAPHIC CORRECTION MODELS IN UAV IMAGES WITH A SPECIAL TARGET

8.1. Context

After the results using field data, it is clear the need to investigate the behavior of those models for different light conditions and different slopes in controlled field campaign, so that we could assess the main factors when applying topographic correction models in real data. To achieve this aim, we planned a field campaign using a specially designed radiometric target, composed by different flat surfaces with selected slopes and took images in eight aspect positions. This data was processed and the topographic correction models were once again applied and analyzed.

8.2. Data acquisition

The field campaign took place in Presidente Prudente, São Paulo state, Brazil, inside the University campus (coordinates -22°07’15.1401”; -51°24’23.6465” SIRGAS2000) on January 18th, 2020. It was summer season and light incidence in the place was high. The time of flight was restricted to cloudless sky, wind gusts of less than 5 m/s, and similar time to usual flights in literature. The location is shown in Figure 21.

Figure 21 Location of field campaign inside university campus

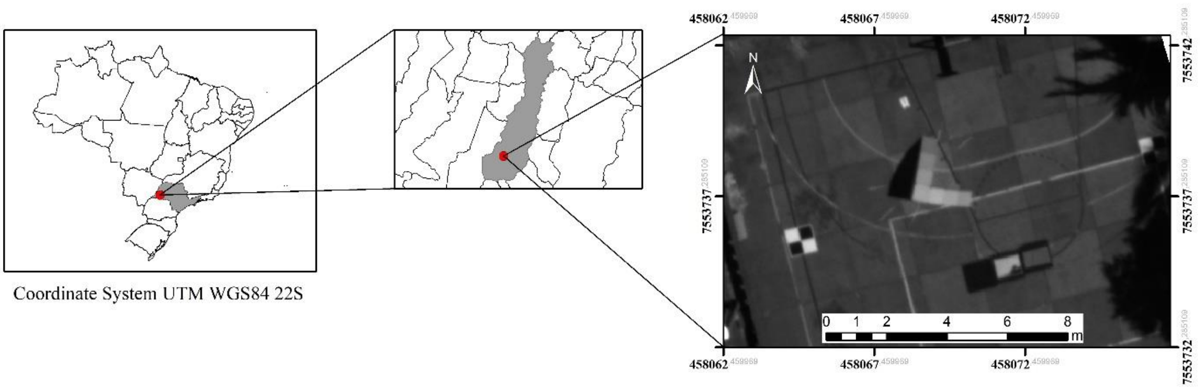

Source: Author

A special radiometric target was built with progressive slope and aspect angles that could appear in real images. From now the target will be mentioned as RT. The RT was built in Medium-density Fiberboard (MDF) boards of 15 mm thickness. It was composed of two perpendicular sets of targets that, when projected horizontally had approximately the same size (0.5 x 0.5 meters). The slope angles are: 0° (plane), 30°, 40° and 70° totalizing 7 targets. Because of the two sets, by rotating the target and maintaining the same rotation axis, it was possible to cover many aspect positions. This radiometric target is shown in Figure 22.

Figure 22 Radiometric Target (RT) used in this work

Source: Author

Three different flights were performed to acquire 4 different positions of the RT regarding the North, in which the sun position and RT position varied. This set of flights was repeated at three different horary (10:30 am, 12:30 pm, and 14:30 pm, local time), using the same flight height of 100m, entailing a 0.03m GSD pixel size.

In flights 1 and 2, the first target location and orientation were intended to point one face as close as possible to the North and the other perpendicular face pointing east. The following positions were made by rotating the RT 30°, 60° and 210° always in clockwise direction, resulting in a 30° increment of the targets for every position. In this way the RT covered 8 azimuth positions in intervals of angles varying from 30° to 90°. For flight number 3, the RT was positioned one face towards north and the other perpendicular face towards west, so that more information about the northwest was available. All the angles are visible in Table

3, and an illustration of the positions is in Figure 23. The positions of the RT are called P1, P2, P3 and P4 for better understanding.

Table 3 Flight data

Position	P1	P2	P3	P4
Time - 1st Flight	10:42	10:47	10:51	10:55
Sun Zenith (°)	26.52	25.36	24.44	23.51
Sun Azimuth (°)	92.01	91.62	91.29	90.95
Time - 2nd Flight	12:20	12:24	12:26	12:31
Sun Zenith (°)	4.02	3.18	2.79	1.94
Sun Azimuth (°)	67.93	61.22	56.43	36.53
Time - 3rd Flight	14:30	14:35	14:40	14:43
Sun Zenith (°)	26.56	27.72	28.87	29.57
Sun Azimuth (°)	268.05	267.66	267.29	267.07

Source: Author

Figure 23 Position of target and Sun at the moment of flights. In first flight Sun is to the east of the target, and in the second flight it is almost Nadir (a). In the third flight the Sun is to the west of the target (b)

(a) (b)

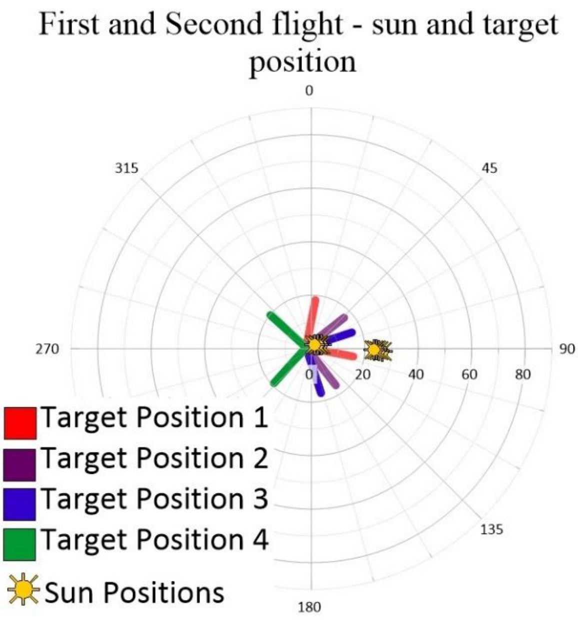

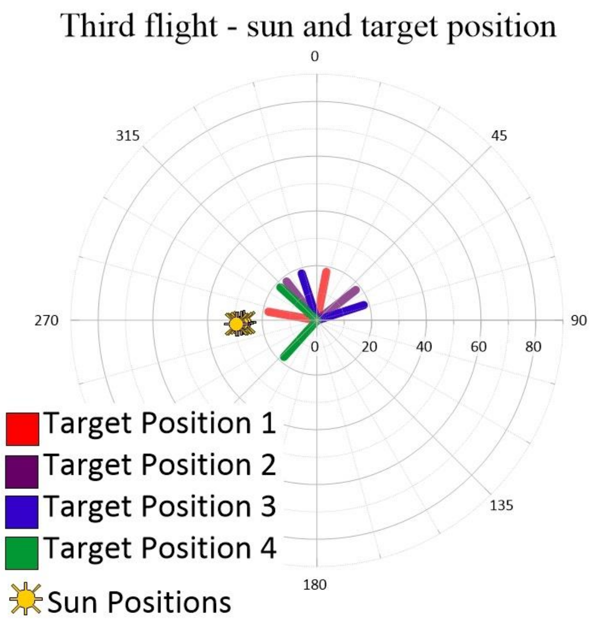

Five bands were selected to be studied: three in the visible range and one in the near infrared (NIR). They are called by B3, B5, B11 and B22 as the order in the hyperspectral cube, and the wavelengths are specified in Table 4.

Table 4 Bands used in the second assessment

Band	Λ (nm)	Description
B3	535.09	Green
B5	565.10	Green
B11	650.39	Red
B22	769.89	Red Edge

Source: Author

For a better understanding of the results, each board of the radiometric target was numbered from 1 to 7 preceded by the letter T. Also, each position the RT had was nominated from 1 to 4, preceded by the letter P, as shows the Figure 24a.

Figure 24 Position of target and targets identification (a) and 3x3 pixel window used to extract targets information (b)

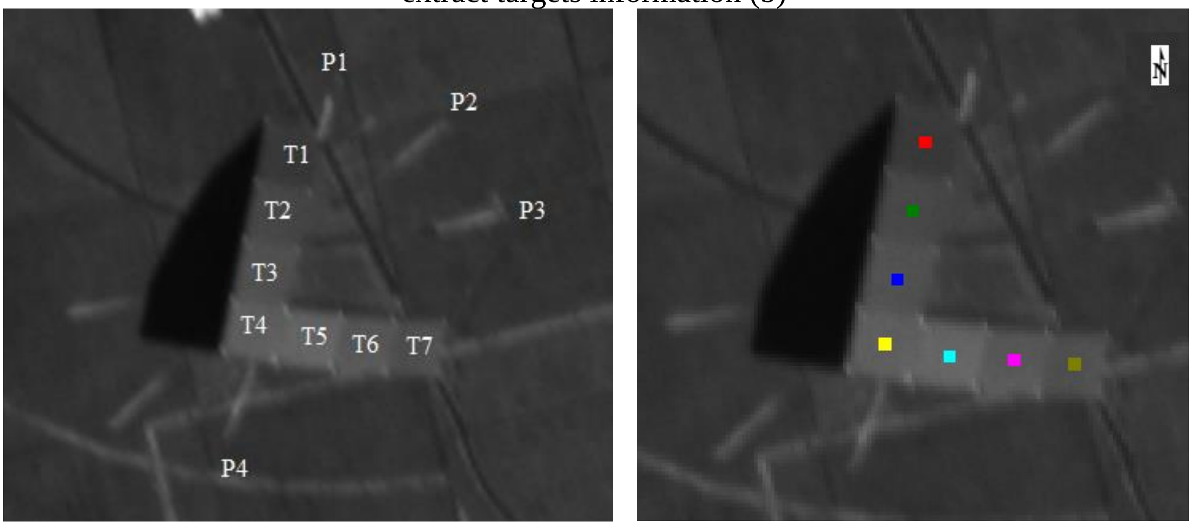

(a) (b)

Source: Author

8.3 Data processing

After acquiring the images, they were georeferenced, corrected from dark current and then transformed form raw DN to radiance using the camera software as described in

Miyoshi *et al*. (2018). Image georeferencing was done with 6 control points in the Global Mapper software (Global Mapper) using a Helmert transformation.

Using local coordinates of the RT a dense point cloud was made using Cloud Compare software. This point cloud was then translated to the real coordinates acquired in situ and rotated to match the respective positions where images were taken. The process of translation and rotation was done using Python IDLE. The dense cloud was then interpolated into a surface using TIN (triangulated irregular network) model in Global mapper. This DSM was merged to the Metashape reference DSM to check over the coordinates and to ensure the DSM had floor data. These steps are illustrated in Figure 25.

Figure 25 Steps to produce the IL image.

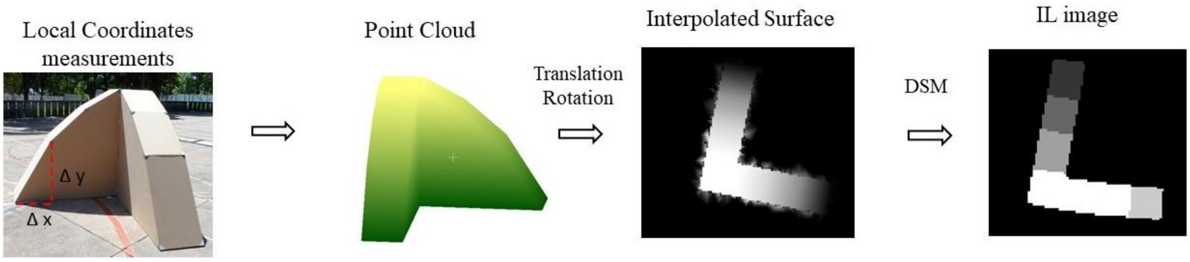

Source: Author

A DSM was produced for each of the positions of the RT, along with data of the sun position, to generate the IL band, as described in Chapter 4. The IL was then used to apply the models to the images. This process is described in the following section.

A 3x3 pixels window was cropped for each slope board and the average values of these 9 pixels window were used to apply the topographic correction models. The radiance values before and after the correction were analyzed.

The data collected was analyzed in 3 different aspects: First, we used numerical results to see the performance of the models, by applying the models to the 3x3 pixel windows. Then, we assessed the performance by means of the standard deviation improvement between each board and finally we applied the models to images to do properly qualitative assess the results.

For the first position, we performed the tests in all four bands in the three flights. As the results were very similar for all the spectra, for the other positions we performed tests for two bands, 5 and 22, which correspond to green and red edge parts of the electromagnetic spectrum.

To properly analyze the results, we calculated the improvement of the standard deviation between the values for each board, considering the best result to be the variance between targets as close to 0 as possible, meaning that the radiance of the target was not depending on the view and illumination geometry. We used the 3x3 pixel window (figure 24b), centered in the board, to extract the mean value of the target radiance. Then, we calculated the standard deviation between the targets (T1 to T7) with no correction (STD_{target}). We applied the models to the mean value of each target and then calculated the standard deviation between the targets again (STD_{model}), using the corrected values by each model. Then, we divided the standard deviation of the corrected values (STD_{model}), by the standard deviation of the non-corrected values (STD_{target}), obtaining the amount of improvement. This is shown in Equation 11.

$$IMPROVEMENT = \left(1 - \frac{STD_{model}}{STD_{target}}\right) * 100 \quad (11)$$

Accordingly, the Improvement is the ratio between the standard deviation after the correction using the proposed model and the standard deviation of the target without correction.

8.4. Results

The results of improvements for Flight1 are presented in Table 5, separated by the position.

For the first flight in the first position, the best results were achieved for B11 (650.39 nm) MOD2, presenting 80.38% of improvement. For the other four bands, the best result was achieved with MOD3, with average improvement of 72% for all bands. For P2, MOD2 and MOD3 presented almost the same performance, with average improvement of 61%. In P3, MOD3 has the best result with average of 74% of improvement. For P4, the models had the worst performance for the first flight, since the best result is for B3 (535.09 nm) with 35% and for B22 (769.89 nm) with 45% of improvement when applying MOD3.

Specifically, for P4 in B3, the worst result is due to the center board (T4 in Figure 24), which corresponds to 0° slope, as seen in Figure 26. For MOD3, the performance would be better excluding board T4. The original value before applying the correction models is shown as "RAD TARGET".

The analysis for each band in each position as a graph is presented in the Appendix A.

Figure 26 Performance of models for Flight1 B3 in P1

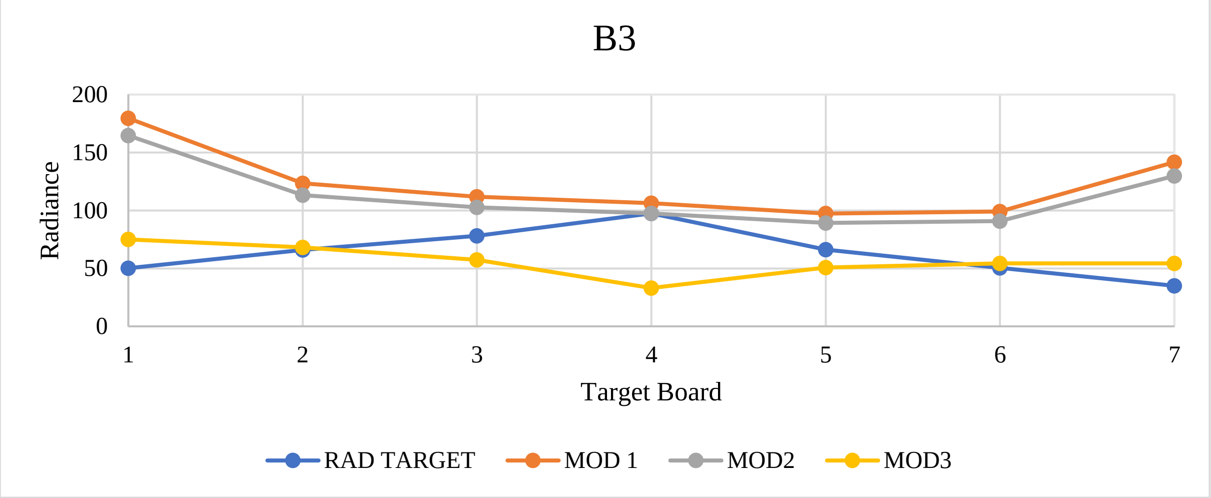

Table 5 Improvement for the Flight1 in all 4 positions.

	IMPROVEMENT P1		
	MOD 1 [%]	MOD2 [%]	MOD3 [%]
B3	58.90	63.22	65.92
B5	67.13	70.58	71.78
B11	78.07	80.38	75.04
B22	67.42	70.85	74.61
	IMPROVEMENT P2		
	MOD1 [%]	MOD2 [%]	MOD3 [%]
B3	52.40	57.35	57.54
B22	62.56	66.45	66.22
	IMPROVEMENT P3		
	MOD1 [%]	MOD2 [%]	MOD3 [%]
B3	63.28	66.57	69.93
B22	79.32	81.17	78.33
	IMPROVEMENT P4		
	MOD1 [%]	MOD2 [%]	MOD3 [%]
B3	-42.85	-30.99	35.19
B22	-11.77	-2.50	44.86

Source: Author

In this flight, Sun elevation angles are very high (23.5° declination from the Nadir) and that makes some targets to be very bright, such as T3, T4 and T5 and some to be very dark such as T7, which is facing the opposite direction. This makes the variability of targets to be very high and explains the negative performance of MOD1 and MOD2 and low performance for MOD3. The negative values represent situations in which the model increased the variance between targets instead of decreasing. This happens because of the calculation of the cosine of illumination, here called IL. Since in MOD1 and MOD2 the IL is used in a division, being the IL the denominator, those cases in which IL is a small number, it turns into a high value of radiance after the model correction, which leads to the increase of the variability between the targets. This will be further explored in the following paragraph.

For this first scenario, we also assessed the influence of the steepest boards in the model performance, by using only the targets T2, T3, T4, T5 and T6 in model 3 (i.e., MOD3), which performed best in almost all cases. Results, here named as MOD3_5, showed poorer results for all bands except for band 11 (Table 6). That result shows that the steeper targets were not influencing the model performance in terms of decreasing the standard deviation between targets.

Table 6 Comparison between MOD3 and MOD3_5 in Flight1, position P1.

IMPROVEMENT P1		
	MOD3 [%]	MOD3_5 [%]
B3	65.92	62.53
B5	71.78	69.93
B11	75.04	78.88
B22	74.61	72.29

For the Flight2, approximate time 12:30, again the same tests were done and the improvements comparison are in Table 7. Results show that in P1, MOD3 had the best performance, showing average performance of 81% for all bands. The best result was achieved for B5 (565.1 nm) (84%) and the worst result was found with MOD1. In P2, P3 and P4 the results were similar, showing good results for MOD3, with almost 90% of improvement for every band, and lowest results for MOD1.

Table 7 Improvement for the Flight2 in all 4 positions.

IMPROVEMENT P1			
	MOD1 [%]	MOD2 [%]	MOD3 [%]
B3	67.66	67.74	83.04
B5	68.98	69.05	84.41
B11	78.07	80.38	75.04
B22	70.23	70.30	83.97
IMPROVEMENT P2			
	MOD1 [%]	MOD2 [%]	MOD3 [%]
B3	71.59	71.63	88.15
B22	81.85	81.88	93.73
IMPROVEMENT P3			
	MOD1 [%]	MOD2 [%]	MOD3 [%]
B3	60.68	60.73	86.03
B22	70.78	70.82	94.14
IMPROVEMENT P4			
	MOD1 [%]	MOD2 [%]	MOD3 [%]
B3	67.01	67.03	87.84
B22	66.05	66.07	88.86

In Flight3, in which the position of target changed, good results were achieved with MOD3 for points P1, P2 and P3. In P4, which was directly pointing the two faces towards the sun, the performance of models was poor, being the maximum for MOD2 and MOD3 varying between 27.7% and 29.10% (Table 8). Although the improvement was not significant, the quality of data was already good, as the values of radiance of boards were similar, presenting small standard deviation (16.18), as shown in Figure 27. All results for individual bands are available in the Appendix A.

Figure 27 Performance of models for B3 in P1 in Flight3

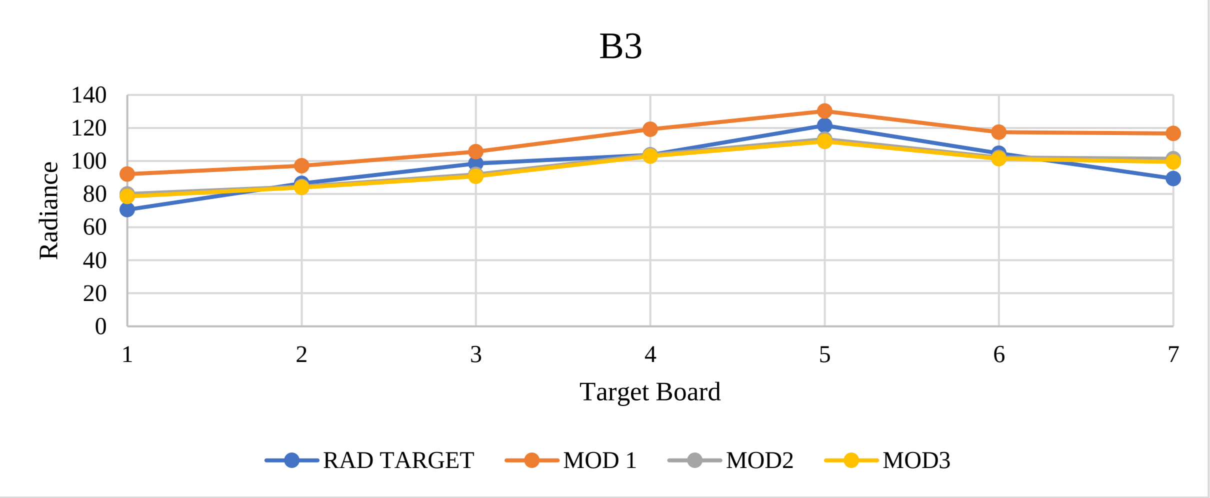

Table 8 Improvement for the Flight3 in all 4 positions.

	IMPROVEMENT P1		
	MOD 1 [%]	MOD2 [%]	MOD3 [%]
B3	63.59	67.44	80.04
B5	56.53	61.12	90.66
B11	72.33	75.25	83.13
B22	59.07	63.39	90.22
	IMPROVEMENT P2		
	MOD 1 [%]	MOD2 [%]	MOD3 [%]
B3	-57.27	-39.22	85.95
B22	-95.67	-73.21	58.51
	IMPROVEMENT P3		
	MOD 1 [%]	MOD2 [%]	MOD3 [%]
B3	-114.05	-87.44	78.17
B22	-229.21	-188.29	72.95
	IMPROVEMENT P4		
	MOD 1 [%]	MOD2 [%]	MOD3 [%]
B3	16.90	27.72	27.90
B22	18.48	29.10	28.94

As pointed before, the variability of radiance between each target was an important parameter to assess the quality of data. Nevertheless, the variability added to data because of inherent characteristics of the Rikola camera must be considered. The way of analyzing this is by the standard deviation of the 3 x 3 pixel window extracted from each target in every flight and position. For all flights and positions, the variability of pixel value in the window is similar, varying from less than 1 unit to about 3. This means that every variation in average of 2 units of radiance should be discredited since it is inherent to the camera noise. The results of standard deviations for the first flight in P1 are shown in Figure 28.

Figure 28 Standard deviation of targets inside the 3 x 3 window in Flight1 P1.

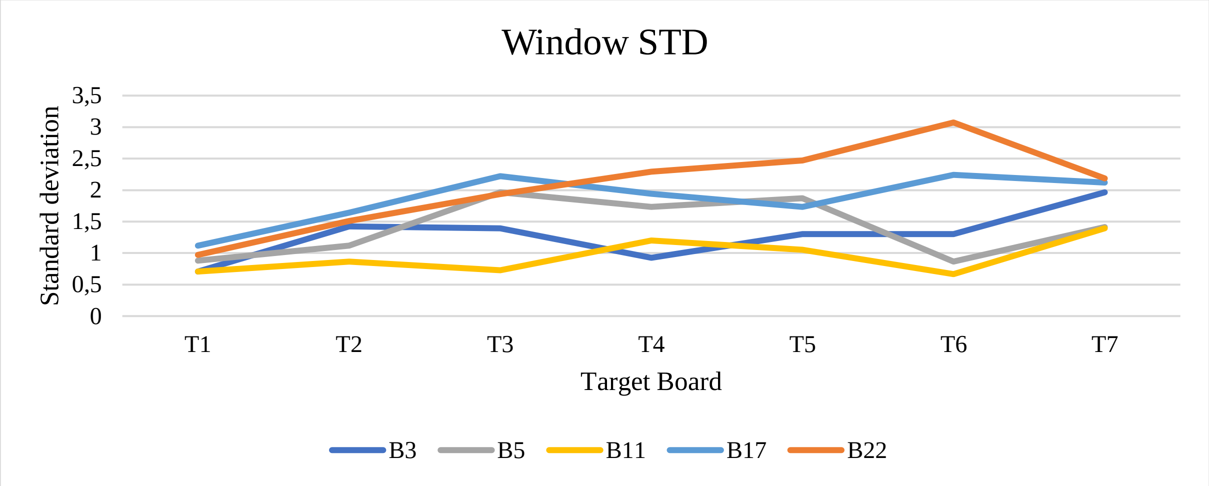

On the other hand, it is important to highlight that the variations analyzed in the brightness improvement previously presented are the standard deviation between each target in a given flight and position. In this case, the standard deviation has higher values and entails the values of performance analyzed before.

The negative values of performance are a result of over correcting a target, which leads to a very high increase of the target radiance value after the correction model and increasing the variability of radiance values among all targets. To assess the situations when this would occur, it is necessary to look closer to the IL equation (Equation (4), section 4.4). It consists of two summed components. The first component results from the multiplication of the cosine of slope ($cos\theta_0$) times the cosine of Sun zenith angle ($cos\theta_n$). The extreme case would happen when the Sun zenith angle is 0, which means at solar noon, or/and if the slope is 0, which would cause this component to be annulated (equal to zero). The IL first component (ILP1) is shown in equation 12.

$$ILP1 = cos\theta_0 cos\theta_n \quad (12)$$

The second component of the IL equation (ILP2) is a multiplication of the sine of slope ($sin\theta_0$) times the sine of sun zenith ($sin\theta_n$), in this case meaning that when the slope of the target approaches 0° and/or the closer the sun is to its peak, this factor tends to be equal to 1. Thus, this factor is multiplied by the sun azimuth angle (ϕ_0) minus the cosine of the aspect angle (ϕ_n). This factor of ILP2 can have a negative result, for those cases in which the sun azimuth angle is smaller than the target aspect. The component portion of IL (ILP2) is shown in equation 13.

$$ILP2 = sin\theta_0 sin\theta_n \cos(\phi_0 - \phi_n) \qquad (13)$$

It is clear that the result with IL would be smaller if the second part of its equation (ILP2) was negative, being the aspect component more important than the slope. This occurred in some examples of our data, such as Flight1 in P4 for all targets except the T4, which is horizontal and, in this case, the ILP2 equals to 0 and the IL is only dependent of the ILP1. Figure 29 shows the relation between the IL value and the target aspect and slope. It is possible to see that the smallest value of IL is achieved for slope equal to 0 rad and for a higher value of aspect, larger than 0.8 rad. The largest value of IL is found when the slope value is higher and the aspect value is lower. In this case, the average value of sun zenith was 0.4 rad and average value of sun azimuth was 1.6 rad.

Teillet *et al*. (1982) already pointed out that the models should work better in slopes of less than 25° (0.43 rad) and IL values of less than 45° (0.78 rad). In our results, we could see that for less sloped targets the models work fine, as already mentioned in the literature, but for our data, with MOD1 and MOD2 the values of IL should have a minimum value either, larger than a maximum value as proposed by the authors.

Figure 29 Values of IL for all positions and all targets in Flight1 related to the target slope and aspect.

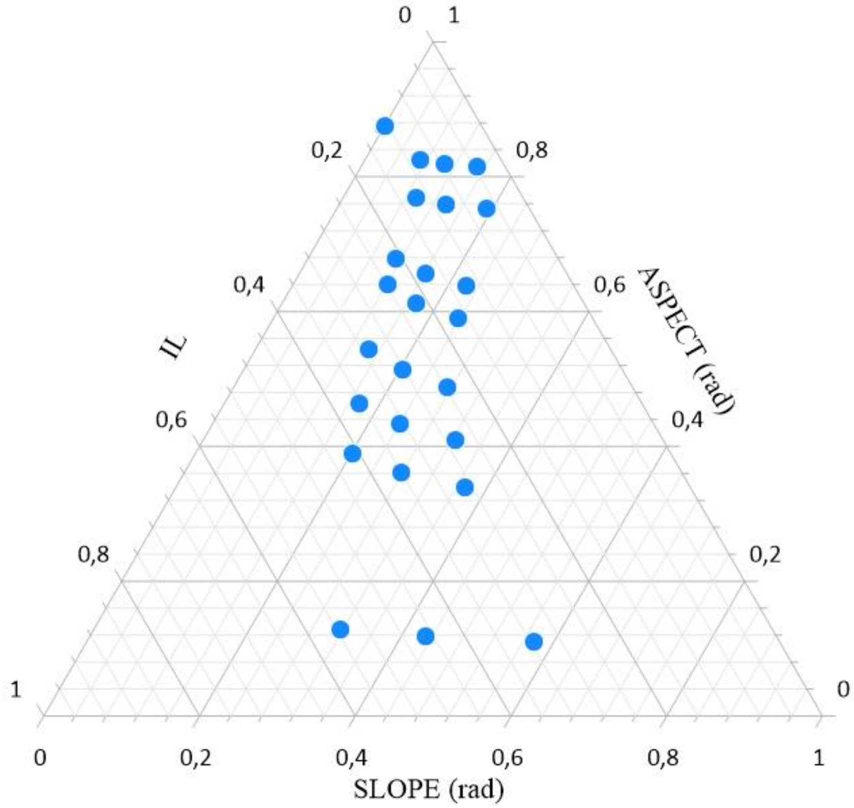

Finally, to show an image resulting of the application of the models, we used the models to correct the images to a qualitative assessment and comparison of the data improvement. As explained before, with exception for some cases where the performance was negative or really small, the results were similar for all bands and all positions. In this sense, we chose to show results only for the Flight1 in P1.

For this purpose, we created an image using numerical IL values previously calculated and used the slope and aspect values from known data from the field campaign. The models were then applied using the raster calculator tool of Envi Software (Harris Geospatial Solutions, Inc.). As expected, it is possible to see that, for some models, the differences between boards are minimized after the topographic correction. It is more noticeable between the first and last targets (T1 and T7), mainly because of the sun position. These results are shown in Figure 30

Figure 30 Performance of models for B3 in P1 for Original data (a), MOD1(b), MOD2(c) and MOD3(d).

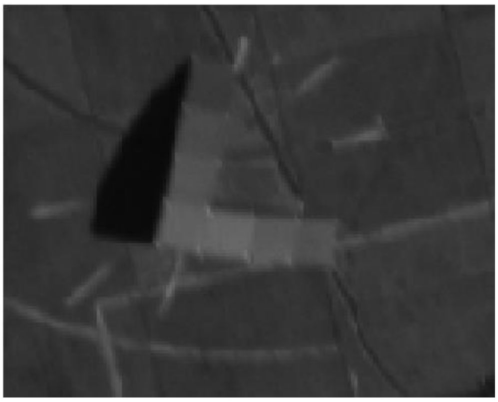

Original (a)

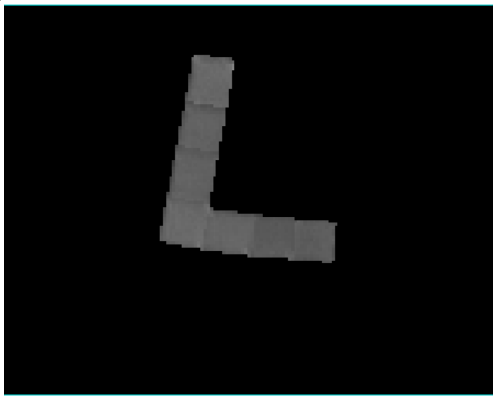

MOD1 (b)

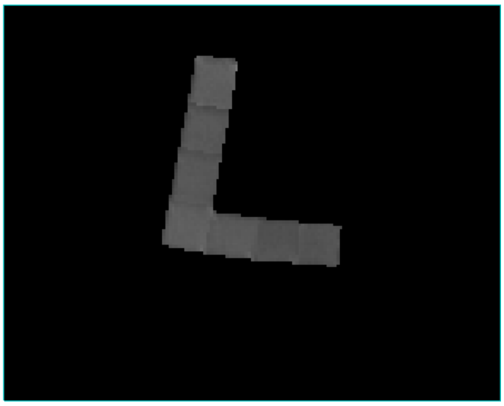

MOD2 (c)

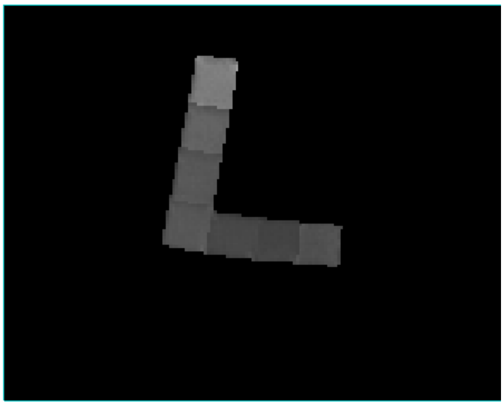

MOD3 (d)

8.5. Partial Analysis

In these experiments we used hyperspectral images of a special target to analyze the performance of three topographic correction models in minimizing the illumination effects in targets radiance caused by different slope and aspect angles

In general, the models had high improvement rates (from 60% to 90%). For most cases, the best results were achieved with model MOD3, which uses the medium value of IL to normalize the corrected irradiance. In cases where the target was pointing to the opposite direction of the sun, MOD 1 and MOD2 had negative improvement, meaning that the model deteriorated the quality of images. We proved that in cases which the value of target's aspect is bigger than the Sun azimuth, the resultant IL may be a small number, precluding the use of models which use the IL as a denominator, because it can increase the variance between lighten and shadowed targets. Also, our work demonstrates that for low solar zenith angles, close to solar noon, the most slopped surfaces (T1 and T7,70° of slope) receive almost one third of the lighting the flat surface would receive (T4), by the cosine of 70º, yet they are corrected in a very good performance.

We used the standard deviation between boards to evaluate the quality of data and this proved to be a good parameter, once it compares the variation of values of the same target, considering the ideal case the one where all boards achieved the same radiance value after topographic correction regardless of its slope and aspect.

Moreover, it is important to highlight the anisotropy of the target. Even using the same target material, the different slope and aspect showed to influence the radiance values of the target. This is more likely to happen in cases when the target is facing the opposite side of the sun. For our data, models that are based in a division between the radiance of target and the IL, if the sun azimuth angle is smaller than the target's slope angle, the outcome is a very bright pixel value and loss of information.

Jakob *et al.* (2017) assessed models in solar zenith of 67° and 36°. For the sun zenith angle of 36°, models performed fine, mostly because the correction effect is low. However, the authors found overcorrection in edges for the MOD3. For sun azimuth angle of 67°, authors had problems in applying the MOD3 in steep shadowed cliffs. Therefore, we notice that the use of the topographic correction models performance is conditioned to the view and lighting geometries, and is important to assess the geometry of sun azimuth angle and the targets aspect, as well as the quality of DSM used to generate the slope and aspect data.

Oliveira *et al.* (2019) shows that some vegetation indices are sensitive to target's slope and aspect, and also shows that to adequately retrieve biochemical and biophysical attributes from vegetation, the topographic correction is necessary, showing the importance of the study of these models in detail.

9. CONCLUSION

Radiometric disturbances caused by illumination are a source of errors in all kinds of remotely sensed data, although they depend on the target location, the geometry formed by sun-target-sensor and the flight height. Due to these variables, it is expected to find different pipelines for different nature of data acquisition, which includes the usual sun position (and consequent illumination geometry) in different latitudes and different variations in the viewing geometries depending on the flight height.

The experiments performed to evaluate the BRDF could only be possible because of the short flight duration (approximately 10 minutes), and, thus, the solar angle can be considered constant for the entire image block. Also, no clouds were covering the area, thus maintaining the same irradiance available.

In our work, we were able to see that the flight with Rikola camera without gimbal stabilization presented small variation in tilt angles in common flight conditions and also that the repeatability of the same geometry for the four targets was small. Thus, it was not feasible to find, besides nadir, a common viewing geometry with varying zenith angle for the same azimuth angle. As a consequence, the ANIX could not be a parameter to compare or distinguish one target from another. Besides, the ANIF shows a random varying behavior, varying in the same ratio for all targets with similar viewing geometries (i.e. excluding dry soil target).

Regarding the Topographic Correction Models applied in field data, we understand that none of them performed effectively for the whole area, but for some targets it showed promising results, as it makes the target more uniform and easier to be distinguished. Because we used field data, composed of irregular microrelief, we could not distinguish the factors that influenced the models when presenting unacceptable results. Hereof, we concluded that besides the models, another important issue was to assess how the DSM can affect the correction model and how it can be used to prevent from over-correction in steep borders such in the limit of sugar cane crop or trees.

Hence, we performed an experiment using a special designed radiometric target to evaluate specific angles and positions and predict the geometry between sun and sensor. In this experiment, three flight times were assessed, four bands in the visible and Red edge wavelengths and four positions of the target per flight time.

Results showed that good results can be achieved for most cases with the analyzed models, even for the steepest boards. This leads us to conclude that the DSM quality in our first experiments, using forest images, was a determinant factor to explain the performance of the topographic correction models.

For our specific data, it is possible to state that the topographic correction model highly improves data quality. It is important to highlight that the variability of spectral response between each target is expected, once it is not a perfect material and as so, the composition may vary and this must be taken into consideration to state that the variability between the targets is acceptable.

In this work, we used data from a hyperspectral camera but we analyzed only few bands because of the high correlation encountered among bands of the same spectrum. Further research would be necessary to confirm the performance of models in a hyperspectral cube.

Further research should be done to assess the performance of topographic correction models with real field data, by improving the IL image generation. Also, tests involving image classification would be a good parameter to assess the improvements produced with topographic correction models in images.

REFERENCES

AASEN, H. *et al.* Generating 3D hyperspectral information with lightweight UAV snapshot cameras for vegetation monitoring: From camera calibration to quality assurance. **ISPRS Journal of Photogrammetry and Remote Sensing**, v. 108, p. 245–259, out. 2015.

BALTHAZAL, V. *et al.* Evaluation and parametrization of ATCOR3 topographic correction method for forest cover mapping in mountain areas. **International Journal od Applied Earth Observation and Geoinformation,** v.18, p. 436-450. Mar 2012

BERVEGLIERI, A.; TOMMASELLI, A. M. G. Exterior Orientation Of Hyperspectral Frame Images Collected With Uav For Forest Applications. **ISPRS - International Archives of the Photogrammetry, Remote Sensing and Spatial Information Sciences**, v. XL-3/W4, p. 45–50, mar. 2016.

BORENGASSER, M.; HUNGATE, W. S.; WATKINS, R**. Hyperspectral Remote Sensing:**
principles and applications. Crc Press Taylor & Francis Group, 2007. 119 p.

BURKART, A. *et al.* Angular Dependency of Hyperspectral Measurements over Wheat Characterized by a Novel UAV Based Goniometer. **Remote Sensing**, v. 7, n. 1, p. 725–746, jan. 2015.

CAMPOS, J. *et al.* Development of canopy vigour maps using UAV for site-specific management during vineyard spraying process. **Precision Agriculture** v.20 p. 1136-1156. Mar 2019

CIVCO, D. L. Topographic normalization of Landsat Thematic Mapper digital imagery. **Photogrammetric Engineering and Remote Sensing**, v. 55, n. 9, p. 1303-1309, sep. 1989.

COLBY, J. D. Topographic Normalization in Rugged Terrain. **Photogrammetric Engineering and Remote Sensing**, v. 57, n. 5, p. 531-537, may 1991.

COLOMINA, I.; MOLINA, P. Unmanned aerial systems for photogrammetry and remote sensing: A review. **ISPRS Journal of Photogrammetry and Remote Sensing**, v. 92, p. 79–97, jun. 2014.

DEL POZO, S. et al. Vicarious Radiometric Calibration of a Multispectral Camera on Board an Unmanned Aerial System. **Remote Sensing,** v. 6, n. 3, p. 1918–1937, mar. 2014.

GINI, R. *et al.* Uav Photogrammetry: Block Triangulation Comparisons. **ISPRS - International Archives of the Photogrammetry, Remote Sensing and Spatial Information Sciences**, v. XL-1/W2, p. 157–162, ago. 2013.

GOVENDER, M.; CHETTY, K.; BULCOCK, H. A review of hyperspectral remote sensing and its application in vegetation and water resource studies. **Water SA**, v. 33, n. 2, p. 145–151, abr. 2007.

GRENZDÖRFFER, G. J.; NIEMEYER, F. Uav Based Brdf-Measurements of Agricultural Surfaces With Pfiffikus In: International Conference On Unmanned Aerial Vehicle In Geomatics (UAV-G) 2011 Zurich, Switzerland. **International Archives of the Photogrammetry, Remote Sensing and Spatial Information Sciences Volume XXXVIII-1/C22** Zurich: ISPRS 2011. 229-234

HONKAVAARA, E. **Calibrating digital photogrammetric airborne imaging systems using a test field**. 2008. Tese (doutorado) - Finnish Geodetic Institute, Finland 2008.

HONKAVAARA, E. *et al.* Digital Airborne Photogrammetry - A New Tool for Quantitative Remote Sensing? -A State-of-the-Art Review On Radiometric Aspects of Digital Photogrammetric Images. **Remote Sensing**, v. 1, n. 3, p. 577–605, set. 2009.

HONKAVAARA, E. *et al.* Processing and Assessment of Spectrometric, Stereoscopic Imagery Collected Using a Lightweight UAV Spectral Camera for Precision Agriculture. **Remote Sensing**, v. 5, n. 10, p. 5006–5039, out. 2013.

HONKAVAARA, E.; KHORAMSHAHI, E. Radiometric Correction of Close-Range Spectral Image Blocks Captured Using an Unmanned Aerial Vehicle with a Radiometric Block Adjustment. **Remote Sensing**, v. 10, n. 2, p. 256, fev. 2018.

IMAI, N. N. *et al.* Analysis of the radiometric response of orange tree crown in hyperspectral UAV images. **The International Archines of the Photogrammetry, Remote Sensing and Spatial Information Sciences.** V. XLII-3/W3. Oct 2017.

IMAI, N.N. *et al.* Shadow detection in hyperspectral images acquired by UAV. **The International Archines of the Photogrammetry, Remote Sensing and Spatial Information Sciences.** V. XLII-2/W13. jun 2019.

IMANGHOLILOO, M. *et al.* Characterizing seedling stands using leaf-off and leaf-on photogrammetric point clouds and hyperspectral imagery acquired from unmaddes aerial vehicle. **Forests** v.10 p.415. 2019

IVUSHKIN, K. *et al.* UAV based soil salinity assessment of cropland. **Geoderma**, v. 338, p. 502–512, mar. 2019.

JAKOB, S.; ZIMMERMANN, R.; GLOAGUEN, R. The Need for Accurate Geometric and Radiometric Corrections of Drone-Borne Hyperspectral Data for Mineral Exploration: MEPHySTo—A Toolbox for Pre-Processing Drone-Borne Hyperspectral Data. **Remote Sensing**, v. 9, n. 1, p. 88, 1 jan. 2017.

JENSEN, J. R. **Sensoriamento remoto do ambiente: uma perspectiva em recursos terrestres**. São José dos Campos: Parêntese, 2011.

KIMES, D. S. Dynamics of directional reflectance factor distributions for vegetation canopies. **Applied optics**, v. 22, n. 9, p. 1364-1372, 1983.

KOUKAL, T.; ATZBERGER, C. Potential of Multi-Angular Data Derived from a Digital Aerial Frame Camera for Forest Classification. **IEEE Journal of Selected Topics in Applied Earth Observations and Remote Sensing**, v. 5, n. 1, p. 30–43, 2012.

LAMBERT, J. H.; ANDING, E. (ERNST). **Photometrie. Photometria, sive De mensura et gradibus luminis, colorum et umbrae (1760)**. Leipzig: W. Engelmann, 1892.

LANDGREBE, D. On Information Extraction Principles for Hyperspectral Data. **Hyperspectral Data Analysis Principles**, p. 34, jul. 1997.

LI, X.; STRAHLER, A. H. Geometric-optical bidirectional reflectance modeling of the discrete crown vegetation canopy: effect of crown shape and mutual shadowing. **IEEE Transactions on Geoscience and Remote Sensing**, v. 30, n. 2, p. 276–292, mar. 1992.

M. TEILLET, P.; GUINDON, B.; GOODENOUGH, D. On the Slope-Aspect Correction of Multispectral Scanner Data. **LARS Symposia**, v. 8, 1 dez. 1982.

MA, L. *et al.* **Using unmanned aerial vehicle for remote sensing application** 21st International Conference on Geoinformatics. **Anais**... *In*: 2013 21ST INTERNATIONAL CONFERENCE ON GEOINFORMATICS. jun. 2013

MANEA, D.;,CALIN, M.A. Hyperspectral imaging in different light conditions. **The Imaging Science Journal.** V. 63 n.4 2015

MIYOSHI, G. T. **Caracterização espectral de espécies de Mata Atlântica de Interior em nível foliar e de copa**. Dissertação (Mestrado em ciências Cartográficas) Faculdade de Ciências e Tecnologia, Presidente Prudente, São Paulo, 2016.

MIYOSHI, G. T. *et al.* Impact of Reduction of Radiometric Resolution in Hyperspectral Images Acquired Over Forest Field. **ISPRS - International Archives of the Photogrammetry, Remote Sensing and Spatial Information Sciences**, v. XLII–1, p. 301–305, sep. 2018.

MIYOSHI, G.T. *et al.*. Comparison of Pixel and Region-Based Approaches for Tree Species Mapping in Atlantic Forest Using Hyperspectral Images Acquired By UAV. **ISPRS - International Archives of the Photogrammetry, Remote Sensing and Spatial Information Sciences**, v. XLII-2/W13, p. 1875–1880, jun. 2019.

MORIYA, E. A. S. *et al.* Detecting Citrus Huanglongbing in Brazilian Orchards Using Hyperspectral Aerial Images. **ISPRS - International Archives of the Photogrammetry, Remote Sensing and Spatial Information Sciences**, v. XLII-2/W13, p. 1881–1886, 5 jun. 2019.

MORIYA, É. A. S.; IMAI, N. N.; TOMMASELLI, A. M. G. A Study on The Effects of Viewing Angle Variation in Sugarcane Radiometric Measures. **Boletim de Ciências Geodésicas**, v. 24, n. 1, mar. 2018.

NEVALAINEN, O. *et al.* Individual tree detection and classification with UAV-based photogrammetry point clouds and hyperspectral imaging. **Remote Sensing** v.9 p.185 **2017**

NICODEMUS, F. E. *et al.* **Geometrical considerations and nomenclature for reflectance**. Gaithersburg, MD: National Bureau of Standards, 1977. Disponível em: <https://nvlpubs.nist.gov/nistpubs/Legacy/MONO/nbsmonograph160.pdf>. Acesso em: 9 jul. 2019.

OLIVEIRA, R. A.de; TOMMASELLI, A.M.G. HONKAVAARA, E. Geometric calibration of a hyperspectral frame camera. **The photogrammetric Record** . V.31 p.325-347. 2016

OLIVEIRA, R. A. DE. **Generation of hyperspectral digital surface model in forest areas using hyperspectral 2D frame camera onboard RPAS**.2017. Tese (Doutorado em Ciências Cartográficas) - Universidade Estadual Paulista, Presidente Prudente, São Paulo jun. 2017.

OLIVEIRA, L.M. de *et al.* Topographic effects on the determination of hyperspectral vegetation indices: a case of study in southeastern Brazil. **Geocarto International** 2019

OSCO, L.P. *et al.* Predicting canopy nitrogen content in citrus-trees using random forest algorithm associated to spectral vegetation indices from UAV-imagery. **Remote Sensing** v.11. p.2925. 2019

PAJARES, G. Overview and Current Status of Remote Sensing Applications Based on Unmanned Aerial Vehicles (UAVs). **Photogrammetric Engineering & Remote Sensing**
Vol. 81, N. 4, April 2015, p. 281–329.

PLAZA, A. *et al.* Recent advances in techniques for hyperspectral image processing. **Remote Sensing of Environment**, Imaging Spectroscopy Special Issue. v. 113, p. S110–S122, 1 set. 2009.

QI, J.; INOUE, Y.; WIANGWANG, N. Hyperspectral Remote Sensing in Global Change Studies. *In*: **Hyperspectral Remote Sensing of Vegetation**. United States: Prasad S. ThenkabailJohn G. LyonAlfredo Huete, 2012. 688p.

ROOSJEN, P. P. J. *et al.* Hyperspectral Reflectance Anisotropy Measurements Using a Pushbroom Spectrometer on an Unmanned Aerial Vehicle—Results for Barley, Winter Wheat, and Potato. **Remote Sensing**, v. 8, n. 11, p. 909, 2 nov. 2016.

ROOSJEN, P.P.J. *et al.* Mapping Reflectance Anisotropy of a Potato Canopy Using Aerial Images Acquired with an Unmanned Aerial Vehicle. **Remote Sensing**, v. 9, n. 5, p. 417, 29 abr. 2017.

SABINS, F. F. **Remote Sensing: Principles and Applications, Third Edition**. [s.l.] Waveland Press, 2007.

SANDMEIER, ST. *et al.* Physical Mechanisms in Hyperspectral BRDF Data of Grass and Watercress. **Remote Sensing of Environment**, v. 66, n. 2, p. 222–233, nov. 1998.

SHAEPMAN-STRUB, G. *et al.* Radiometry and Reflectance: From Terminology Concepts to Measured Quantities. *In*: **The SAGE Handbook of Remote Sensing**. [s.l.] SAGE, 2009. p. 539.

SELLERS, W.D**. Physical Climatology.** University of Chicago Press, Chicago 1965

SMITH, G. M.; MILTON, E. J. The use of the empirical line method to calibrate remotely sensed data to reflectance. **International Journal of Remote Sensing**, v. 20, n. 13, p. 2653–2662, jan. 1999.

SMITH, J.A.; LIN, T.L.; RANSON, K.J. The Lambertian Assumption and Landsat Data. **Photogrammetric Engineering and Remote Sensing**, v. 46, n. 9, p. 1183-1189, sep. 1980

SOLA, I. *et al.* Synt4etic images for evaluating topographic correction algorithms. **IEEE transactions on geoscience and remote sensing.** V.52.no.3.2014

TMUSIC, G. *et al.* Current Practices in UAS-based environmental monitoring. **Remote Sensing.** V.12 p.1001. 2020

VILJANEN,N. *et al.* A novel machine learning method for estimanting biomass of grass swards using a photogrammetric canopy height model, images and vegetation indices captured by a drone. **Agriculture** .v.8 p.70. 2018

WATTS, A. C.; AMBROSIA, V. G.; HINKLEY, E. A. Unmanned Aircraft Systems in Remote Sensing and Scientific Research: Classification and Considerations of Use. **Remote Sensing**, v. 4, n. 6, p. 1671–1692, jun. 2012.

YAO, H.; QIN, R.; CHEN, X. Unmanned Aerial Vehicle for Remote Sensing Applications -A Review. **Remote Sensing**, v. 11, n. 12, p. 1443, jan. 2019.

ZHANG, L. *et al.* An analysis of shadow effects on spectral vegetation indexes using a ground-based imaging spectrometer. **IEEE Geoscience and Remote Sensing letters.** V.12 no.11. 2015

APPENDIX A – MODELS PERFORMANCE FOR EACH FLIGHT AND EACH POSITION

In this work we assessed three different topographic correction models, in three flights and in four different positions. The topographic correction is described in item 4.4 of our work. The models are named here as MOD1, MOD2 and MOD3 as the following Table 1, and as explained in item 4.6 of our work.

Table 1 Models of Topographic correction applied in this preliminary test

Model	Reference	Equation
MOD1	Simple Ratio	$L_C = \frac{L_0}{IL}$
MOD2	Cosine	$L_C = L_0 \frac{\cos(\theta_0)}{IL}$
MOD3	Normalized	$L_C = L_0 \frac{ILm - IL}{ILm}$

Source: Author

Flights were named as Flight1, Flight2 and Flight3 in the ascending order of the time of flight. Also, in each flight the Radiometric Target (RT) is positioned in 4 positions, here called P1, P2, P3 and P4. The time of flights is available in table 3, item 8.2 of the work. Also, it is possible to visualize the positions of the RT in Figure 23 of our work, in item 8.2.

In this appendix we present the performance for each flight and position of the RT in three models. For the first positions we assessed the performance of models in 4 bands, named B3 (535.09 nm), B5 (565.10 nm), B11 (650.39 nm) and B22 (769.89 nm). For positions P2, P3 and P4 only bands B3 and B22 were assessed because the behavior of models in all wavelengths is similar.

In all figures of this appendix, the curve RAD TARGET stands for the value of radiance of the target before the correction of each model, and is the mean value of a 3x3 pixel window. The TR is divided in 7 targets, here enumerated from 1 to 7, like shown in Figure 24 of our work. Therefore, the abscissa axis represents the seven targets and the ordinate axis stands for the radiance value.

1. Results for Flight1 in P1

Fig. Ap 1 Performance of MOD1, MOD2 and MOD3 for B3 in Flight1 P1

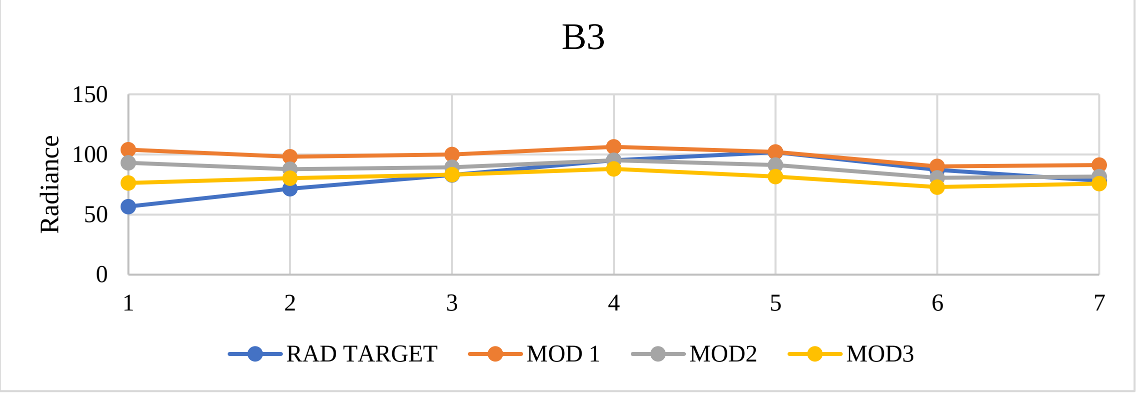

Fig. Ap 2 Performance of MOD1, MOD2 and MOD3 for B5 in Flight1 P1

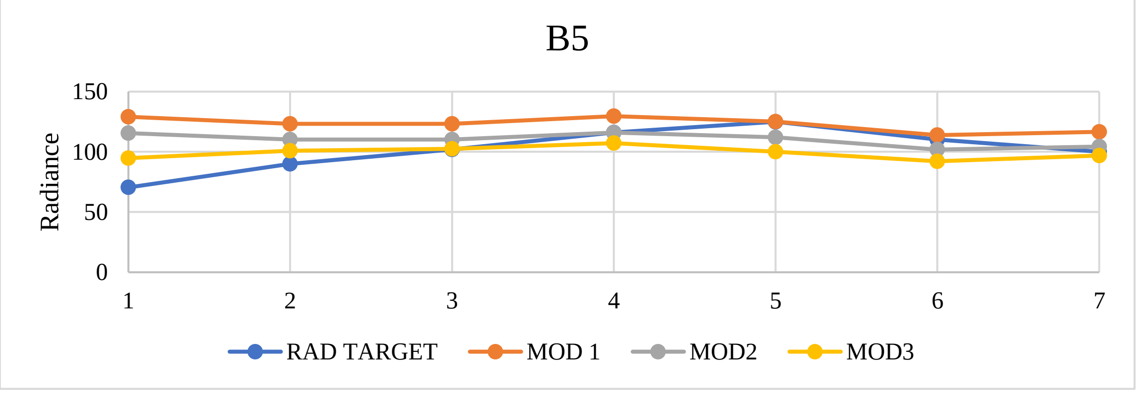

Fig. Ap3 Performance of MOD1, MOD2 and MOD3 for B11 in Flight1 P1

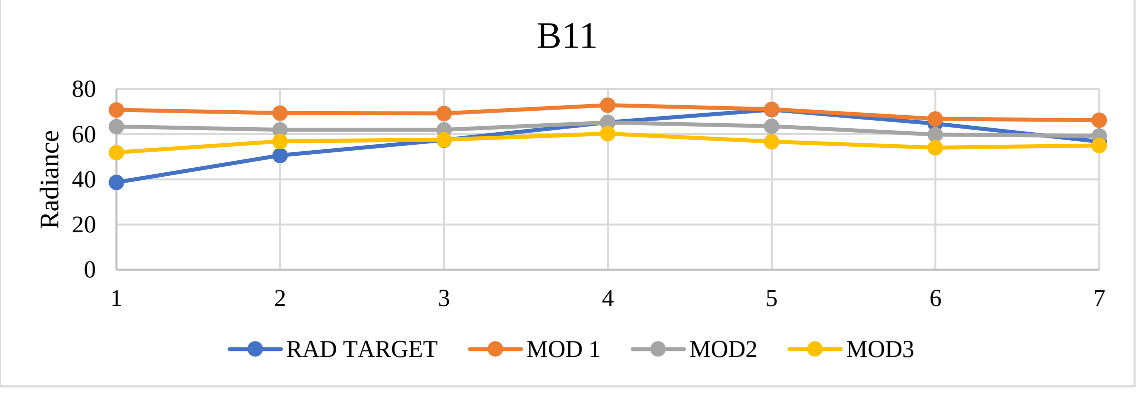

Fig. Ap 4 Performance of MOD1, MOD2 and MOD3 for B22 in Flight1 P1

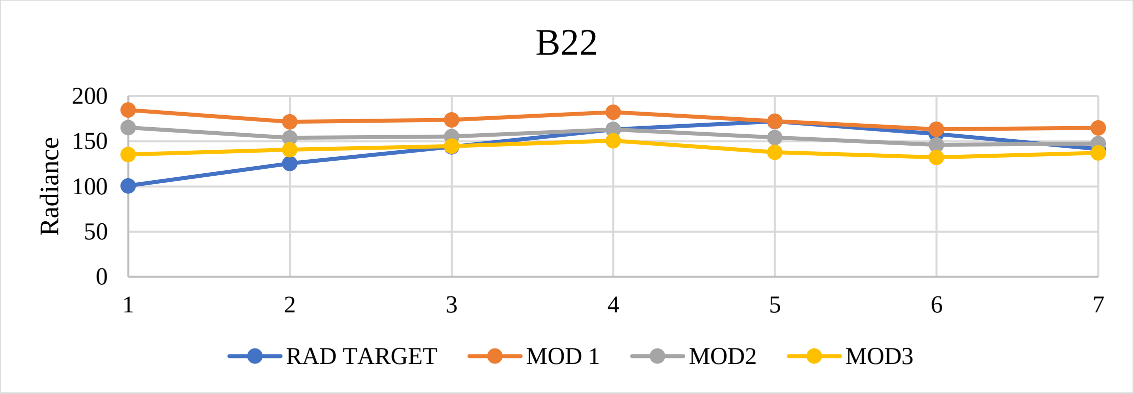

2. Results for Flight1 in P2

Fig. Ap 5 Performance of MOD1, MOD2 and MOD3 for B3 in Flight1 P2

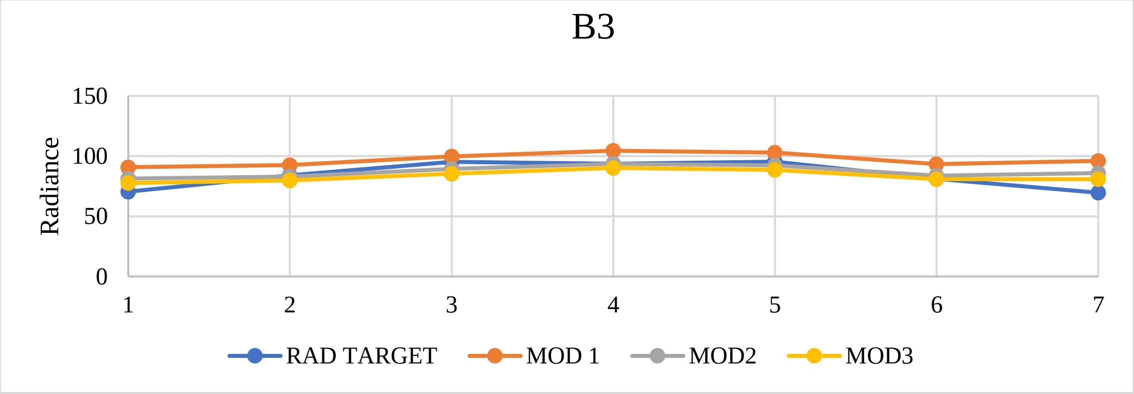

Fig. Ap 6 Performance of MOD1, MOD2 and MOD3 for B22 in Flight1 P2

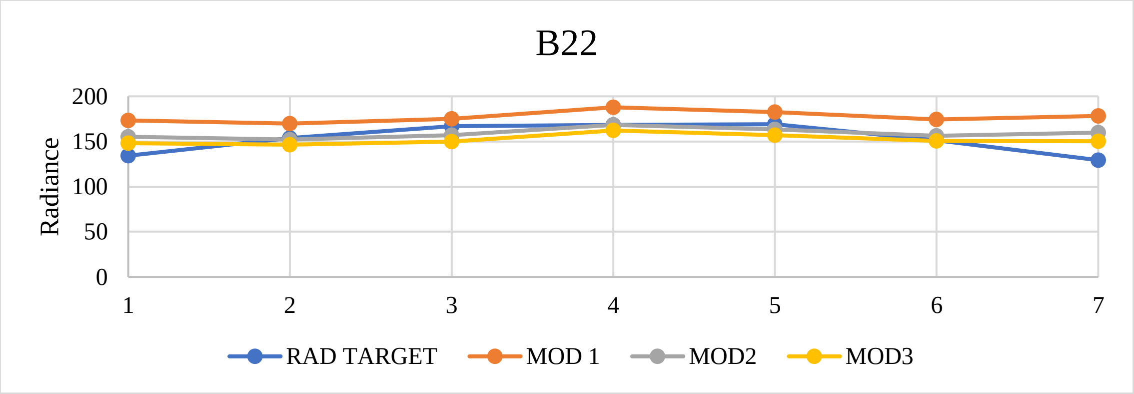

3. Results for Flight 1 P3

Fig. Ap 7 Performance of MOD1, MOD2 and MOD3 for B3 in Flight1 P3

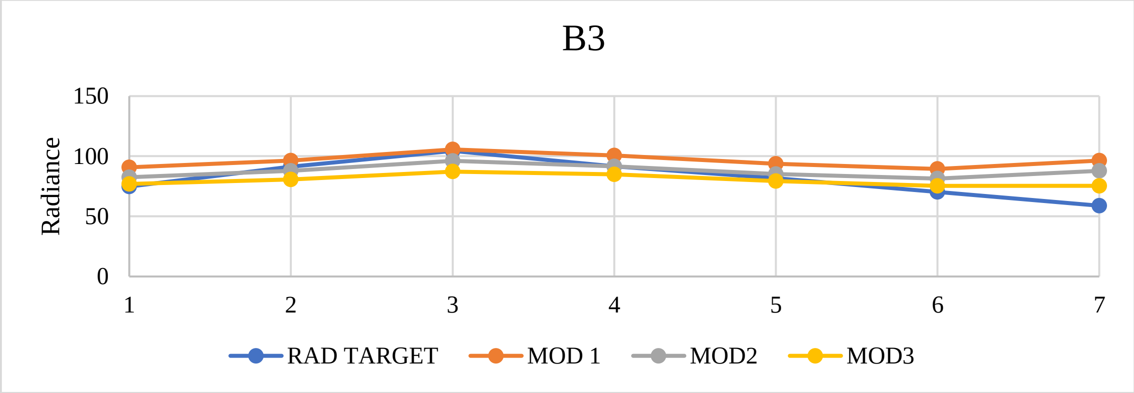

Fig. Ap 8 Performance of MOD1, MOD2 and MOD3 for B22 in Flight1 P3

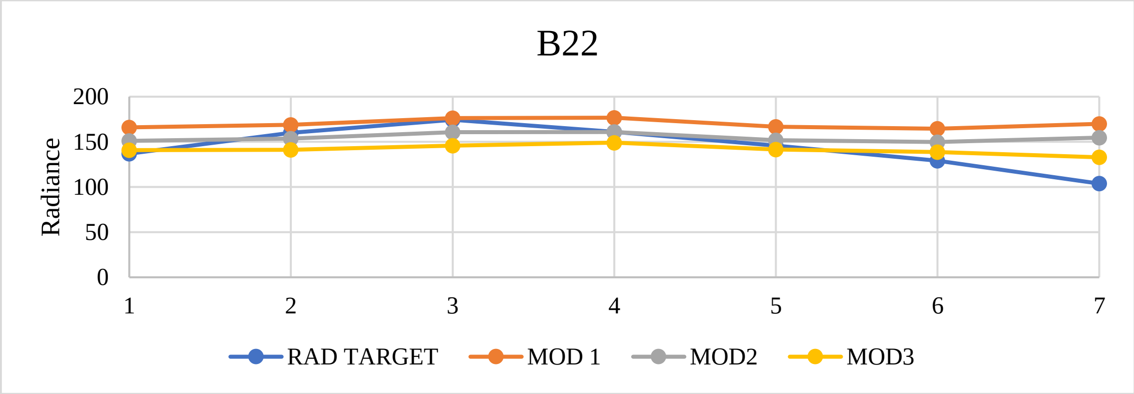

4. Results for Flight 1 P4

Fig. Ap 9 Performance of MOD1, MOD2 and MOD3 for B3 in Flight1 P4

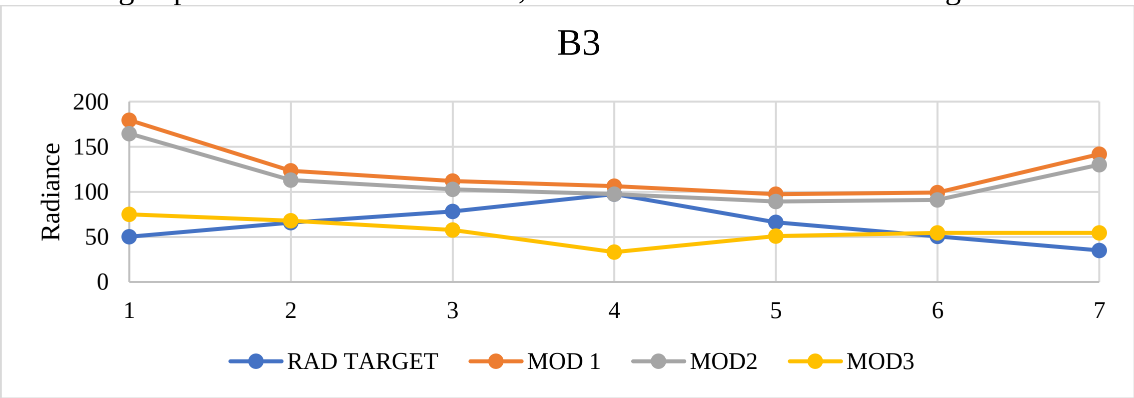

Fig. Ap 10 Performance of MOD1, MOD2 and MOD3 for B22 in Flight1 P4

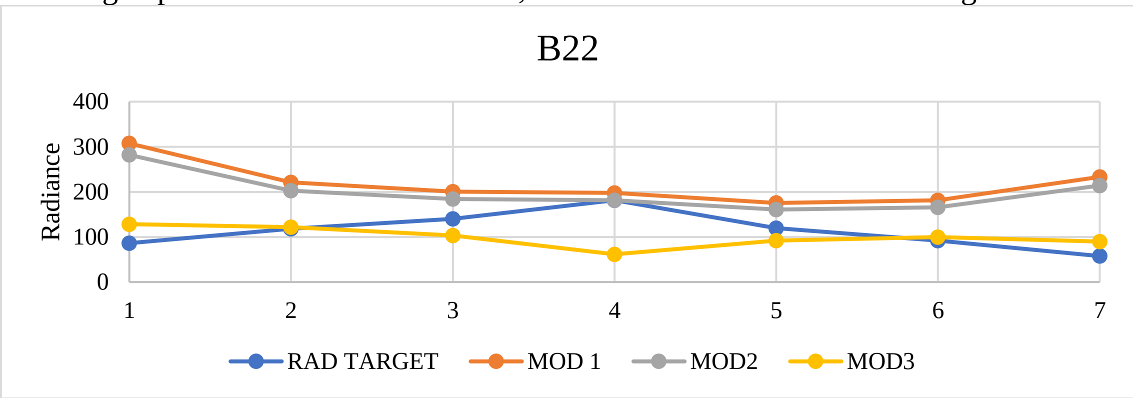

5. Results for Flight 2 P1

Fig. Ap 11 Performance of MOD1, MOD2 and MOD3 for B3 in Fligh2 P1

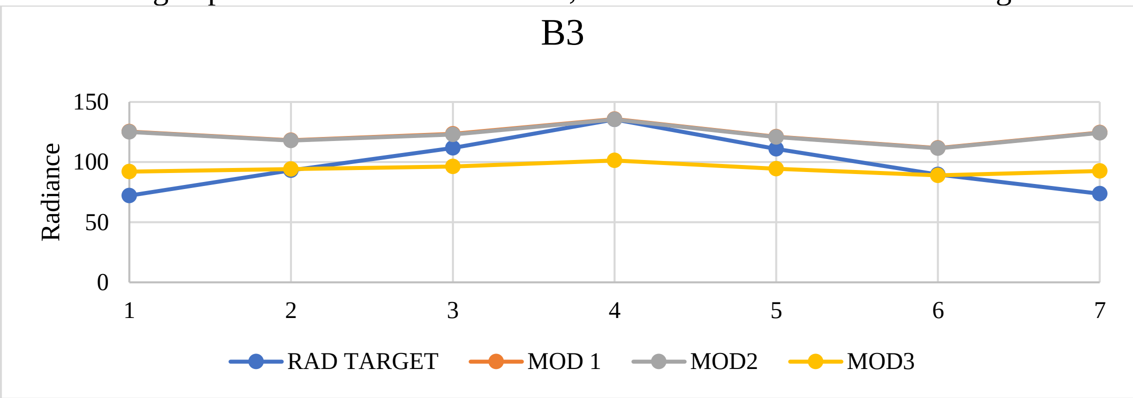

Fig. Ap 12 Performance of MOD1, MOD2 and MOD3 for B5 in Fligh2 P1

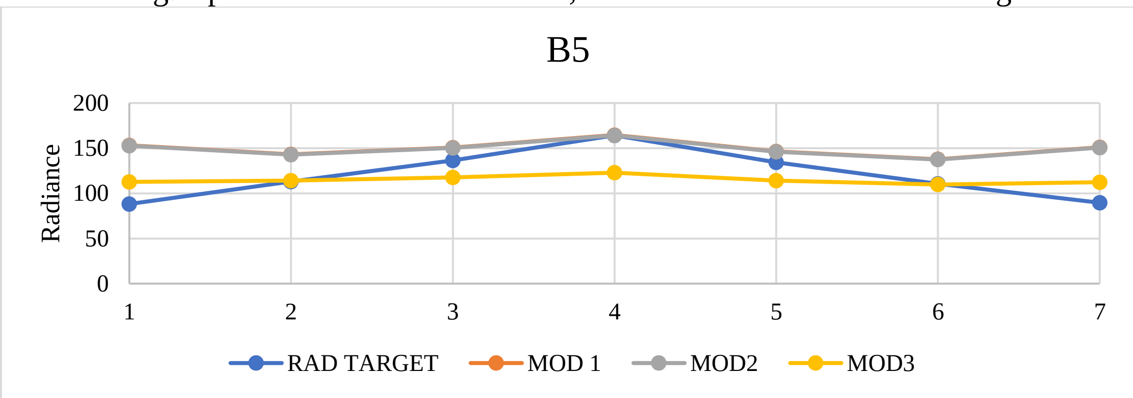

Fig. Ap 13 Performance of MOD1, MOD2 and MOD3 for B11 in Fligh2 P1

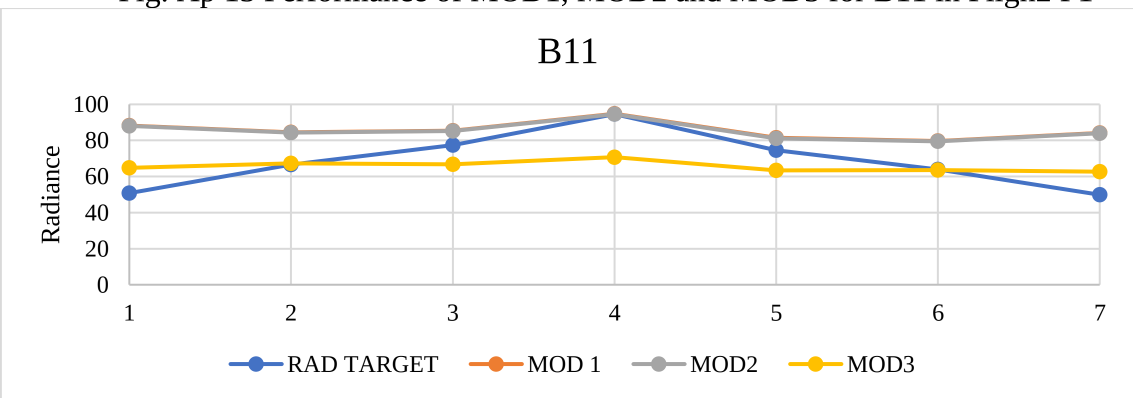

Fig. Ap 14 Performance of MOD1, MOD2 and MOD3 for B22 in Fligh2 P1

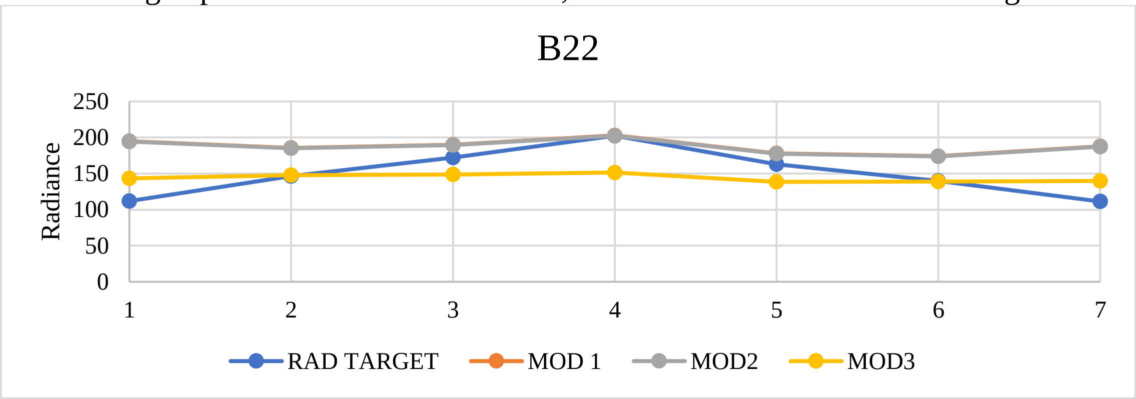

6. Results for Flight 2 P2

Fig. Ap 15 Performance of MOD1, MOD2 and MOD3 for B3 in Fligh2 P2

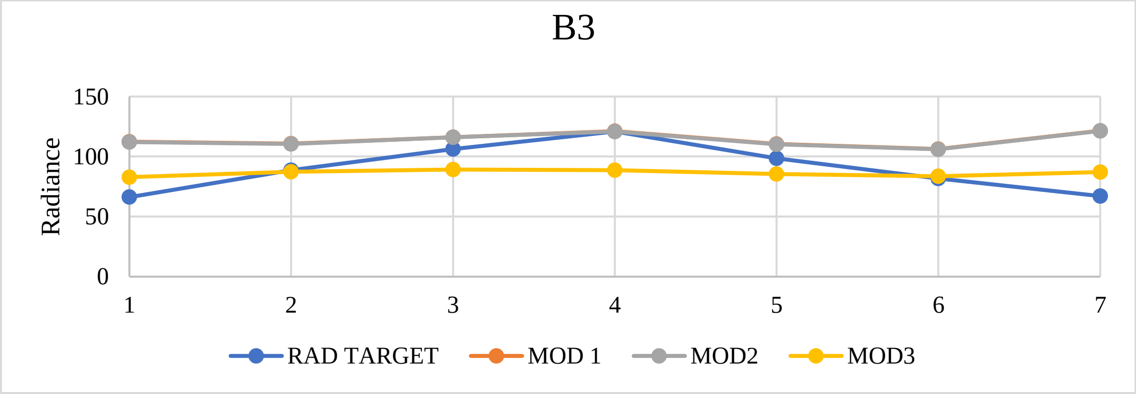

Fig. Ap 16 Performance of MOD1, MOD2 and MOD3 for B22 in Fligh2 P2

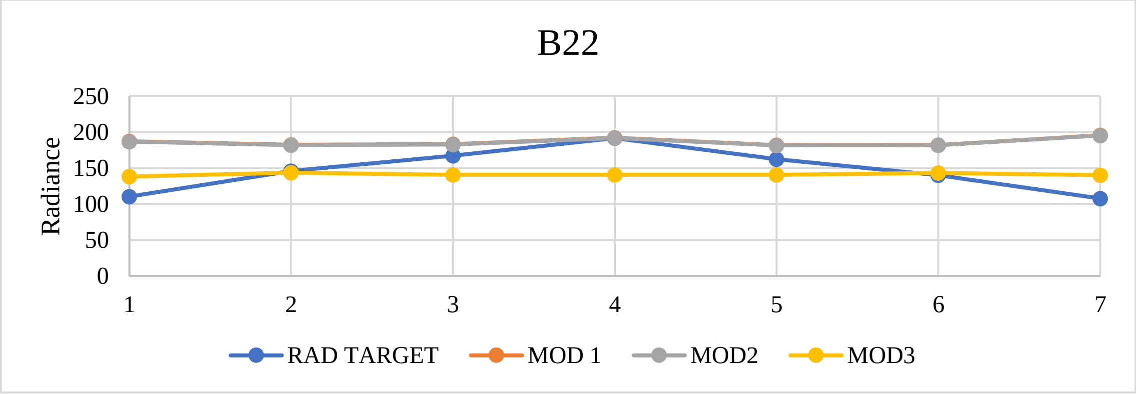

7. Results for Flight 2 P3

Fig. Ap 17 Performance of MOD1, MOD2 and MOD3 for B3 in Fligh2 P3

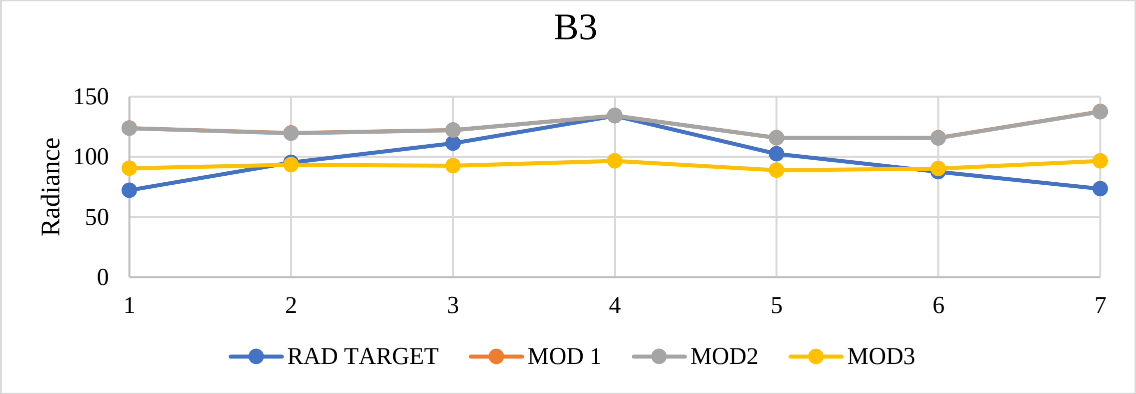

Fig. Ap 18 Performance of MOD1, MOD2 and MOD3 for B22 in Fligh2 P3

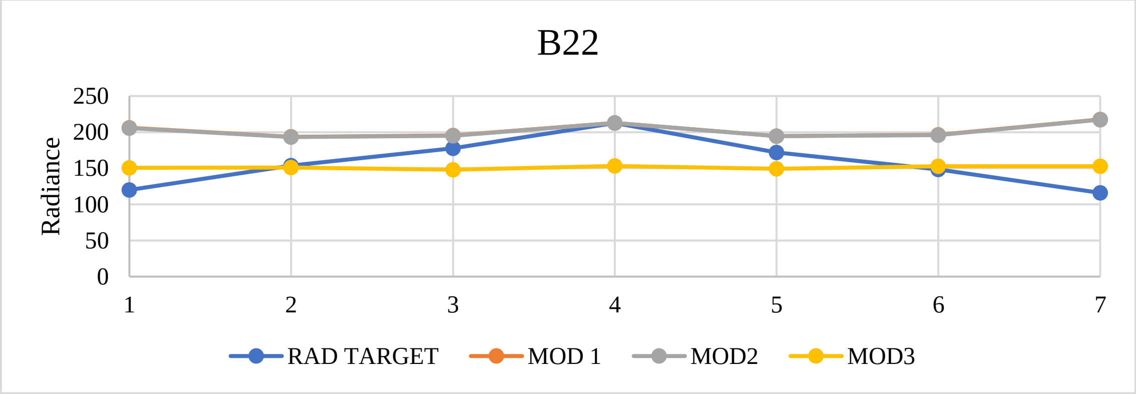

8. Results for Flight 2 P4

Fig. Ap 19 Performance of MOD1, MOD2 and MOD3 for B3 in Fligh2 P4

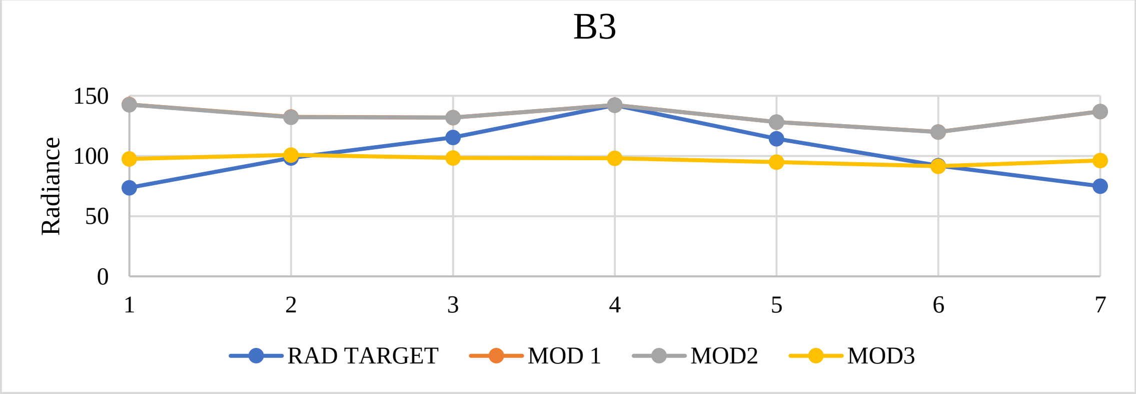

Fig. Ap 20 Performance of MOD1, MOD2 and MOD3 for B22 in Fligh2 P4

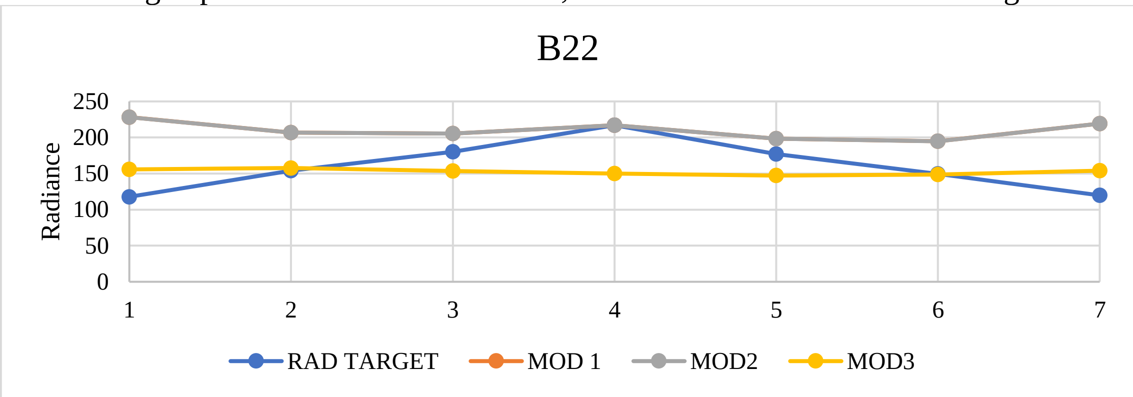

9. Results for Flight 3 P1

Fig. Ap 21 Performance of MOD1, MOD2 and MOD3 for B3 in Fligh3 P1

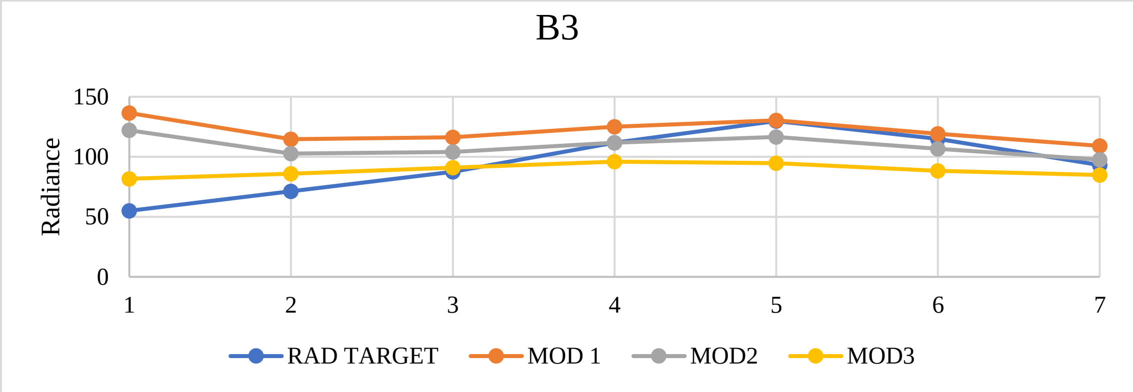

Fig. Ap 22 Performance of MOD1, MOD2 and MOD3 for B5 in Fligh3 P1

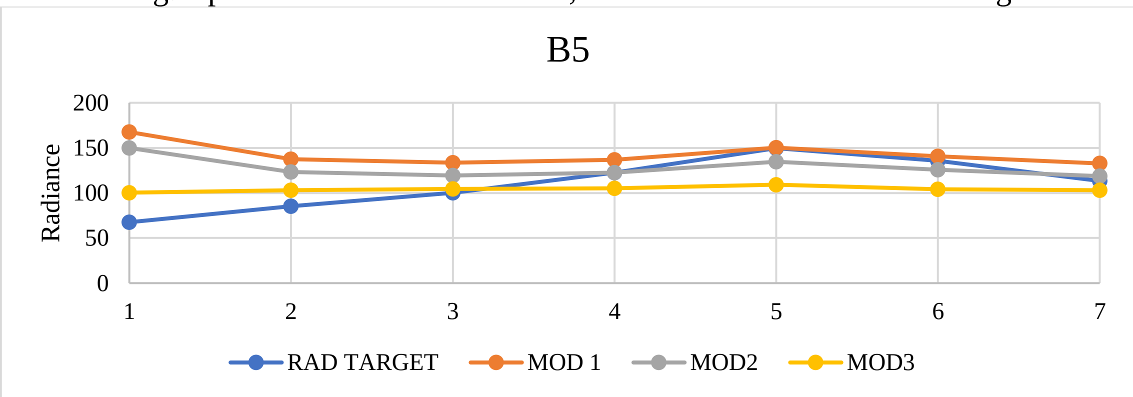

Fig. Ap 23 Performance of MOD1, MOD2 and MOD3 for B11 in Fligh3 P1

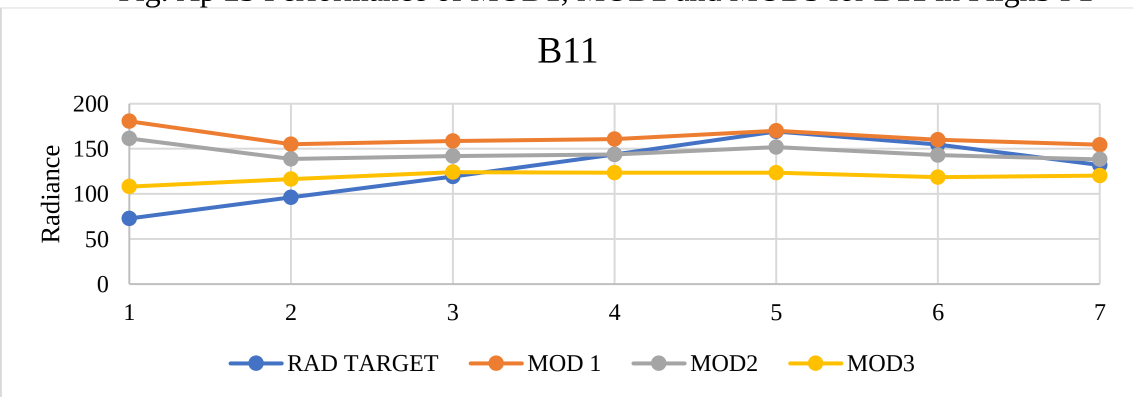

Fig. Ap 24 Performance of MOD1, MOD2 and MOD3 for B22 in Fligh3 P1

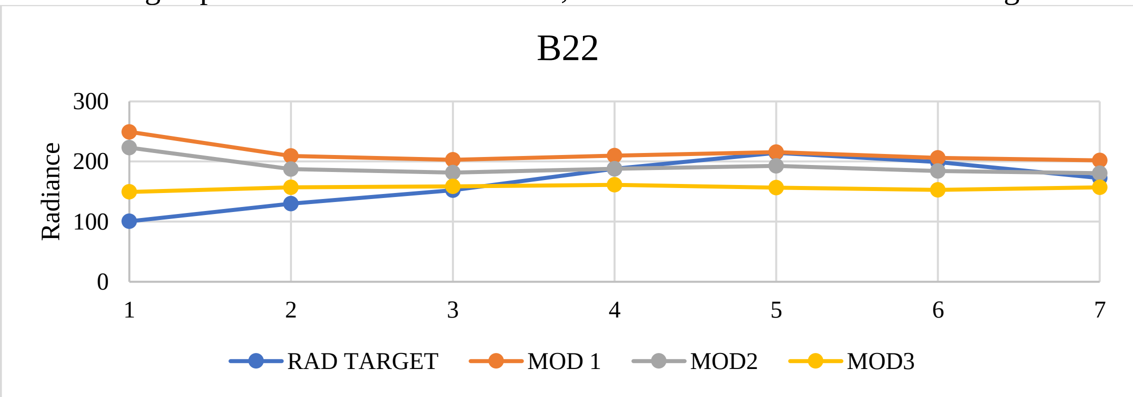

10. Results for Flight 3 P2

Fig. Ap 25 Performance of MOD1, MOD2 and MOD3 for B3 in Fligh3 P2

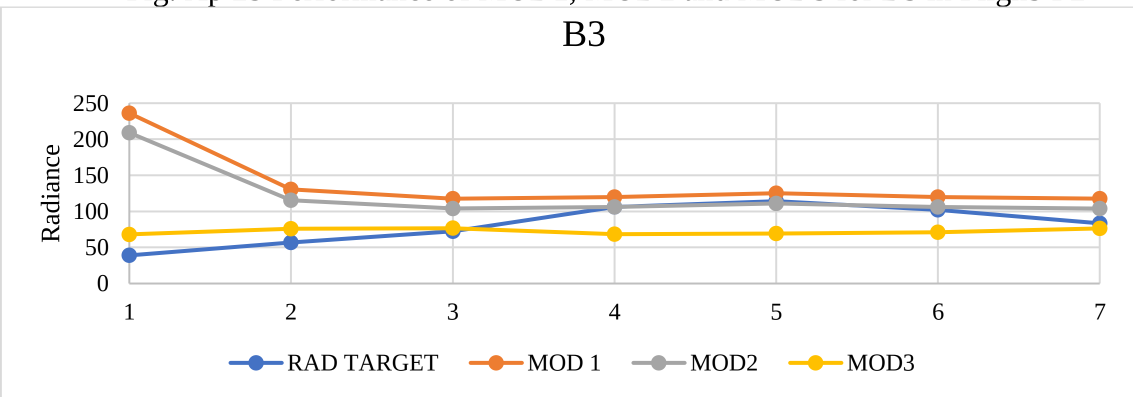

Fig. Ap 26 Performance of MOD1, MOD2 and MOD3 for B22 in Fligh3 P2

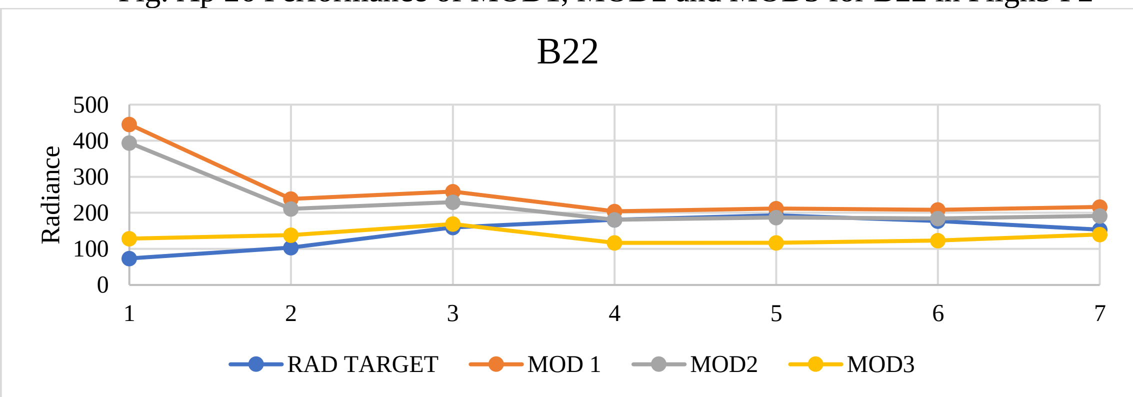

11. Results for Flight 3 P3

Fig. Ap 27 Performance of MOD1, MOD2 and MOD3 for B3 in Fligh3 P3

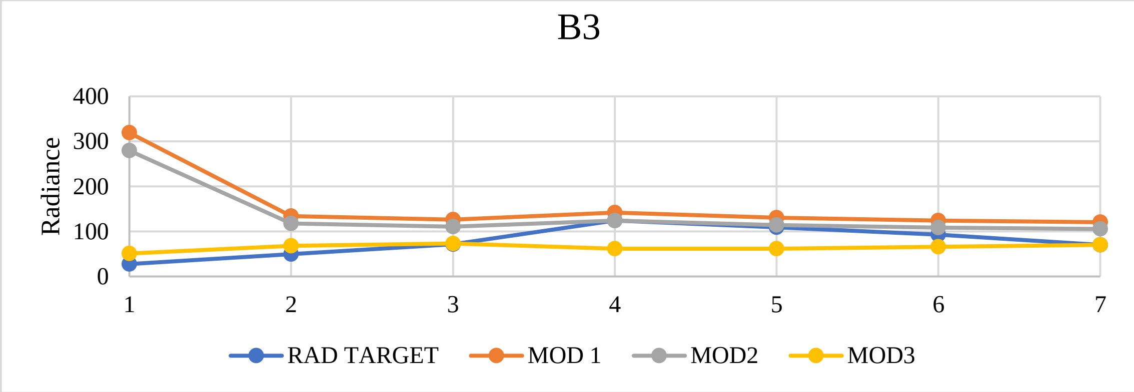

Fig. Ap 28 Performance of MOD1, MOD2 and MOD3 for B22 in Fligh3 P3

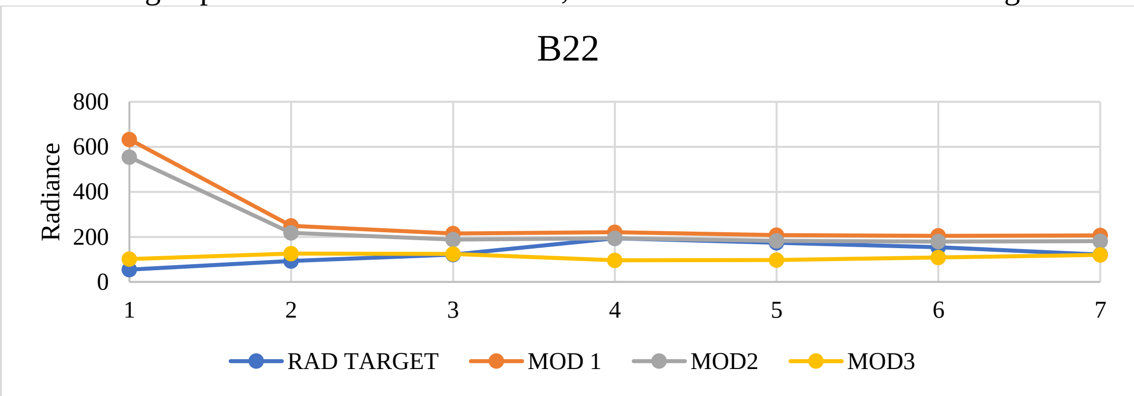

12. Results for Flight 3 P4

Fig. Ap 29 Performance of MOD1, MOD2 and MOD3 for B3 in Fligh3 P4

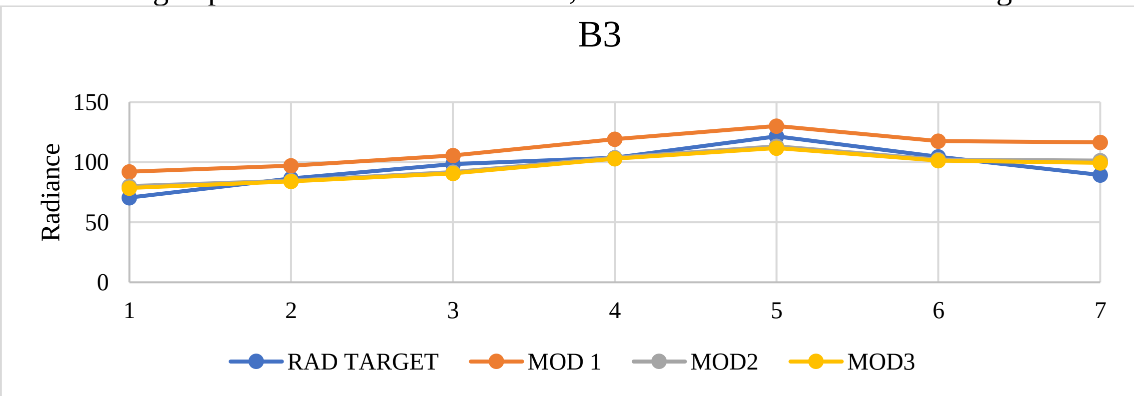

Fig. Ap 30 Performance of MOD1, MOD2 and MOD3 for B22 in Fligh3 P4